NAVAL POSTGRADUATE SCHOOL

MONTEREY, CALIFORNIA

THESIS

DESIGN AND TESTING OF A MULTI-UNIT PAYLOAD DELIVERY AND TRACKING SYSTEM FOR GUIDED MUNITIONS TO COMBAT UAV SWARM THREATS

by

Robert C. Thyberg II

June 2019

Thesis Advisor: Christopher M. Brophy
Co-Advisor: David F. Dausen

THIS PAGE INTENTIONALLY LEFT BLANK

REPORT DOCUMENTATION PAGE			*Form Approved OMB No. 0704-0188*

1. AGENCY USE ONLY *(Leave blank)*	**2. REPORT DATE** June 2019	**3. REPORT TYPE AND DATES COVERED** Master's thesis

4. TITLE AND SUBTITLE DESIGN AND TESTING OF A MULTI-UNIT PAYLOAD DELIVERY AND TRACKING SYSTEM FOR GUIDED MUNITIONS TO COMBAT UAV SWARM THREATS	**5. FUNDING NUMBERS**
6. AUTHOR(S) Robert C. Thyberg II	
7. PERFORMING ORGANIZATION NAME(S) AND ADDRESS(ES) Naval Postgraduate School Monterey, CA 93943-5000	**8. PERFORMING ORGANIZATION REPORT NUMBER**
9. SPONSORING / MONITORING AGENCY NAME(S) AND ADDRESS(ES) N/A	**10. SPONSORING / MONITORING AGENCY REPORT NUMBER**

11. SUPPLEMENTARY NOTES The views expressed in this thesis are those of the author and do not reflect the official policy or position of the Department of Defense or the U.S. Government.

12a. DISTRIBUTION / AVAILABILITY STATEMENT Approved for public release. Distribution is unlimited.	**12b. DISTRIBUTION CODE** A

13. ABSTRACT (maximum 200 words)

A growing problem facing national security revolves around inexpensive, easily manufactured drones. Sophisticated software can link drones into swarms and inflict heavy damage on the United States and her allies' assets, while rudimentary drones could also be used by terrorists to strike civilians from afar. Current defenses against drone swarms are conventional missiles that can cost hundreds of thousands of dollars; the disproportion in cost is not in U.S. favor. The NPS Rocket Propulsion Lab has explored the design of a low-cost delivery vehicle capable of deploying multiple guided munitions laterally out of the missile body at an altitude greater than that of the drone swarm. The guided munitions would be tasked by a targeting hub that would remain aloft above the specific drones, providing unique guidance commands to each deployed unit. This thesis focused on the deployment of the munitions from a flight system, utilizing both Computational Fluid Dynamics and real flight testing to design an effective ejection mechanism and tracking approach. Additionally, high-level design and analysis of a targeting system within the missile was performed. Although there are many solutions being explored to this pressing problem, this thesis seeks to give the United States more cost-symmetric options and capabilities when it comes to air defense against drone swarms in the future.

14. SUBJECT TERMS anti-swarm, delivery vehicle, drone swarm, UAV swarm, guided munition, defense, cost-asymmetry, low-cost	**15. NUMBER OF PAGES** 119
	16. PRICE CODE

17. SECURITY CLASSIFICATION OF REPORT Unclassified	**18. SECURITY CLASSIFICATION OF THIS PAGE** Unclassified	**19. SECURITY CLASSIFICATION OF ABSTRACT** Unclassified	**20. LIMITATION OF ABSTRACT** UU

NSN 7540-01-280-5500

Standard Form 298 (Rev. 2-89)
Prescribed by ANSI Std. 239-18

THIS PAGE INTENTIONALLY LEFT BLANK

Approved for public release. Distribution is unlimited.

DESIGN AND TESTING OF A MULTI-UNIT PAYLOAD DELIVERY AND TRACKING SYSTEM FOR GUIDED MUNITIONS TO COMBAT UAV SWARM THREATS

Robert C. Thyberg II
Ensign, United States Navy
BS, U.S. Naval Academy, 2018

Submitted in partial fulfillment of the
requirements for the degree of

**MASTER OF SCIENCE IN ENGINEERING SCIENCE
(AEROSPACE ENGINEERING)**

from the

**NAVAL POSTGRADUATE SCHOOL
June 2019**

Approved by: Christopher M. Brophy
Advisor

David F. Dausen
Co-Advisor

Garth V. Hobson
Chair, Department of Mechanical and Aerospace Engineering

THIS PAGE INTENTIONALLY LEFT BLANK

ABSTRACT

A growing problem facing national security revolves around inexpensive, easily manufactured drones. Sophisticated software can link drones into swarms and inflict heavy damage on the United States and her allies' assets, while rudimentary drones could also be used by terrorists to strike civilians from afar. Current defenses against drone swarms are conventional missiles that can cost hundreds of thousands of dollars; the disproportion in cost is not in U.S. favor. The NPS Rocket Propulsion Lab has explored the design of a low-cost delivery vehicle capable of deploying multiple guided munitions laterally out of the missile body at an altitude greater than that of the drone swarm. The guided munitions would be tasked by a targeting hub that would remain aloft above the specific drones, providing unique guidance commands to each deployed unit. This thesis focused on the deployment of the munitions from a flight system, utilizing both Computational Fluid Dynamics and real flight testing to design an effective ejection mechanism and tracking approach. Additionally, high-level design and analysis of a targeting system within the missile was performed. Although there are many solutions being explored to this pressing problem, this thesis seeks to give the United States more cost-symmetric options and capabilities when it comes to air defense against drone swarms in the future.

THIS PAGE INTENTIONALLY LEFT BLANK

TABLE OF CONTENTS

LIST OF FIGURES

THIS PAGE INTENTIONALLY LEFT BLANK

LIST OF TABLES

THIS PAGE INTENTIONALLY LEFT BLANK

LIST OF ACRONYMS AND ABBREVIATIONS

3-D	Three-dimensional
AI	Artificial intelligence
AFRL	Air Force Research Laboratory
AGL	Above ground level
ATR	All thread rod
AWG	American wire gauge
CAVR	Center for Autonomous Vehicle Research
C_d	Drag Coefficient
CETC	China Electronics Technology Group
CFD	Computational fluid dynamics
CO_2	Carbon dioxide
COTS	Commercial-off-the-shelf
CRUSER	Consortium for robotics and unmanned systems education and research
DARPA	Defense Advanced Research Projects Agency
FAR	Friends of Amateur Rocketry
FOV	Field of view
GM	Guided munition
in	inch
lbf	pound-force
LED	Light-emitting diode
LiPo	Lithium-Polymer
mm	millimeter
MSL	mean sea level
NPS	Naval Postgraduate School
Pa	Pascal
PLA	Polylactic Acid
psi	pounds per square inch
psig	pounds per square inch gauge
RAF	Royal Air Force

RCAF	Royal Canadian Air Force
RDE	rotating detonation engine
RPL	Rocket Propulsion Laboratory
SRM	Solid rocket motor
SUAVE	Small unmanned aerial vehicle eliminator
UAV	Unmanned aerial vehicle
WAF	Wrap-around fins

ACKNOWLEDGEMENTS

I would like to thank Dr. Brophy and the staff of the NPS Rocket Propulsion Lab for their continued support and assistance during the entirety of this project. The RPL staff, specifically Robert Wright, Dave Dausen, Josh Codoni, and Lee Van Houtte, helped out immensely during every stage of my project, and I value their insight and mentorship. Thank you.

Thank you to LT Matt Busta, USN, and Capt Keith Lobo, RCAF, for your steady guidance into the ways of the Rocket Lab; any question I had was generously answered. I also must thank the team of friends who supported me through this process and helped me still see the sunshine every day: Kayla, Taco, Boone, and all those who helped. Monterey, specifically the Goat house, feels like home. All of the members of N831, especially Jake and Tony, got me up every morning and defined what a strong community looks like. These memories and friendships won't be quickly forgotten.

I very much appreciate being given the opportunity to study at NPS and thank those who had a hand in creating and furthering the Shoemaker Scholarship. I recognize the great opportunity I've been given to design and build my own rocket, and will always fondly remember the time spent launching rockets in the Mojave Desert.

THIS PAGE INTENTIONALLY LEFT BLANK

I. INTRODUCTION

A. BACKGROUND

The ever-changing front of warfare rewards the belligerents that recognize the advantages of emerging technologies and successfully implement new ideas before their adversaries. Examples can be found throughout every human conflict; results were immediate in recent conflicts such the Second World War, where advances in communications and nuclear research were harnessed by the Allied forces and used to asymmetrically shift the tide towards victory. Alan Turing's improvements to algorithmic code-breaking at Bletchley Park assisted in deciphering German communications, work that the Imperial War Museum estimates saved millions of lives and shortened the war by several years [1]. Similarly, the Manhattan Project combined efforts of scientists, industrialists, and engineering to create nuclear weapons that led to the Japanese surrender in 1945 [2].

The impact of technology in warfare lies in the asymmetry it produces between belligerents. Turing's work created an asymmetric communication network as German U-boat communications could be intercepted by the British analysts, while Allied plans such those for Operation Overlord (D-Day) remained in secrecy [3]. The first use of an atomic bomb at Hiroshima in 1945 was also undeniably asymmetric; the Axis powers had no nuclear capability to retaliate with, despite their own research efforts. These examples demonstrate the importance of maintaining technological superiority over an adversary at all times, and highlight the cost of having no suitable response or defense in the event an adversary gains an asymmetric advantage.

Recent leaps in drone swarm technologies present a similar opportunity for asymmetric advantages over adversaries, as drones can be linked into swarms and autonomously make decisions from shared information [4]. The implications of drone swarm technology are vast and potentially devastating, especially coupled with artificial intelligence research which could minimize the necessity for humans in the loop. Intelligent drone swarms have the potential to affect every facet of warfare from reconnaissance and

intelligence gathering to ballistic missile defense, and even kinetic strikes upon an adversary. Research into harnessing drone swarm technology for military assets is well underway, and has been for several years. Project Gremlins, a Defense Advanced Research Projects Agency (DARPA) and the Air Force Research Lab (AFRL) initiative, seeks to "project volleys of low-cost, reusable systems over great distances and retrieve them in mid-air" [5]. DARPA's research, shown in Figure 1, in addition to micro-drone tests from the U.S. Navy and Air Force, are stepping stones to realizing drone swarm usage in a conventional warfare scenario [6].

Figure 1. DARPA and AFRL's Project Gremlins concept. Source: [5].

Autonomous drone swarms as an offensive military asset is an important futuristic goal for the U.S. and her allies in the coming few years, however research into swarm defense capabilities is just as necessary, and arguably more timely. China's state-owned technology company CETC continues to make advances in swarm technology, overseeing in June 2017 a test of 119 fixed-wing UAVs (unmanned aerial vehicles) engaged in complex formations [7]. Their motivations for swarm research are not veiled: Chinese Aerospace Knowledge magazine chief editor Wang Yanan hints that UAV research has

huge potential in military affairs and "will change the ways wars are fought" [8]. The Center for a New American Security (CNAS), a Washington, D.C.-based think tank, characterizes the CETC swarm threat as entirely military in nature:

> These intelligent unmanned systems could serve as an asymmetric means through which to target high-value U.S. weapons platforms, including fighter jets or aircraft carriers. Of note, China's Military Museum includes in one exhibit a depiction of a UAV swarm combat system with swarms used for reconnaissance, jamming, and 'swarm assault' targeting an aircraft carrier. [9]

Fully autonomous drone swarms in warfare are not the current reality, but swarm demonstrations such as those performed by the CETC indicate the potential destruction even rudimentary built and controlled drones can cause if outfitted with incendiary payloads. This extends the threat to non-state actors and terrorists with access to relatively inexpensive microprocessors and UAV parts coupled with the desire to wreak havoc by remote-control.

B. MOTIVATION

The true asymmetry that drone swarms create at present is with regards to cost. An inexpensive, rudimentary swarm in the hands of a terror organization could cause damage that rivals a sophisticated weapon system at a fraction of the cost. The problem lies in the defense against these threats; the novelty of swarms in warfare have led to inexpensive UAVs and payloads typically being countered by large, multi-million dollar missile defense systems. Speaking at the Association of the U.S. Army's Global Force symposium in March of 2017, General David Perkins spoke of a U.S. ally that combatted small quadrotor UAVs with a $3.4 million Patriot missile. He identified the "gut instinct" to use conventional weapons since "that's an air defense problem, because they're in the air," and classified the problem as an economically disparity as opposed to a capability disparity [10]. More recently, two Russian bases in Syria were attacked by Syrian rebels using a "swarm" of 13 UAVs in early January 2018. The UAVs were equipped with explosive payloads, however were extremely crude and consisted of a lawnmower engine and assorted parts wrapped in plastic tape [11]. The UAVs used in the attack are shown in Figure 2. The 13 drones were hesitantly called a "swarm" due to the lack of artificial

intelligence (AI) driving the system; each UAV was GPS guided to the target [11]. Russian defense systems neutralized seven of the UAVs using the Pantsir-S1 air defense system (Figure 2), while six UAVs required complex electronic attack countermeasures to down [12].

Figure 2. Russian Pansir-S1 air defense system (Left) and rudimentary Syrian UAV used in 2018 attack (Right). Sources: [13] and [12].

Although the attack was not a sophisticated and cutting-edge demonstration of AI in warfare, the Russian defense highlights the extreme cost asymmetry emerging to combat even "dumb" drone conglomerations: a Pantsir missile system is a highly technical defense weapon that costs $15 million per unit that fires both surface-to-air missile and 30 mm anti-aircraft cannons [13] was used to eliminate UAVs assembled at a fraction of the price. A monumental price disparity coupled with evidence that anti-aircraft systems struggle to defeat swarms in general levels the playing field for adversaries with less technical ability and minimal access to sophisticated weapons. This growing threat must be managed through the development of lower-cost UAV and swarm defense systems to ensure that sophisticated U.S. military assets are being preserved for symmetrical threats. A state or non-state actor that recognizes this weakness in U.S. defense could potentially bleed U.S. resources using rudimentary UAV conglomerations. Once sophisticated AI-driven drone swarms become a reality on the battlefield, U.S. defenses will be severely exposed if solutions have not been generated.

C. OBJECTIVES AND APPROACH

One subset of the Naval Postgraduate School (NPS) Rocket Propulsion Laboratory (RPL) has been sponsored by the NPS Foundation and has focused on designing, building, and testing a low-cost delivery vehicle to combat enemy drone swarms. One prototype, the Small Unmanned Aerial Vehicle Eliminator (SUAVE), has been generated through the work of two previous theses [14], [15], and continues to be developed through specific research and design of each subsystem. Captain Kai Grohe of the Royal Canadian Air Force (RCAF) assumed the role of missile chief designer and constructed a working, broad-level missile intercept vehicle implemented with a solid rocket motor (SRM) for propulsion, anti-roll capabilities, and satisfactory controllability [14]. Captain Grohe worked on each subsystem at the surface level and transformed the SUAVE from a rough concept to a solid framework from which each subsequent subsystem could be adequately designed in the future. Captain Keith Lobo, RCAF, further shaped the program by determining the intercept concept of operations and designing kill mechanism used to neutralize the swarm threat [15]. The general concept of operations of the proposed SUAVE vehicle is shown below in Figure 3.

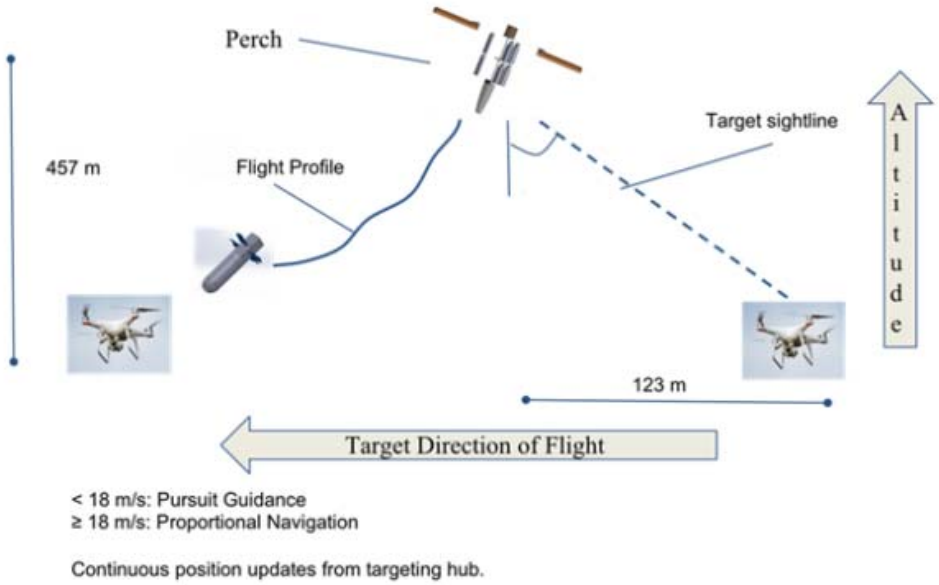

Figure 3. SUAVE concept of operations. Source: [15].

The SUAVE would launch when a swarm was detected and calculate a trajectory to reach apogee between 457 meters (1,500 feet) and 1219.2 m (4000 ft) above the swarm. At apogee, the SRM stage separation would occur and the upper stage, consisting of a targeting hub and GM bay, would rotate 180˚ and begin descent under parachute. The vehicle would contain multiple guided munitions (GMs) used for neutralizing the threat which would be deployed laterally out of the GM bay. Once deployed, the GMs would be continually receiving guidance instructions for swarm intercept from the targeting hub, the delivery vehicle nose cone under canopy that acts as the eye in the sky. The drone swarm kill mechanism designed by Captain Lobo incorporated a Dyneema net that engulfed the threat UAV [15]. The current GM prototype used for analysis was designed by Robert Wright of the NPS RPL and is shown below in Figure 4. The intercept concept of operations depicting deployment to target neutralization is shown in Figure 5.

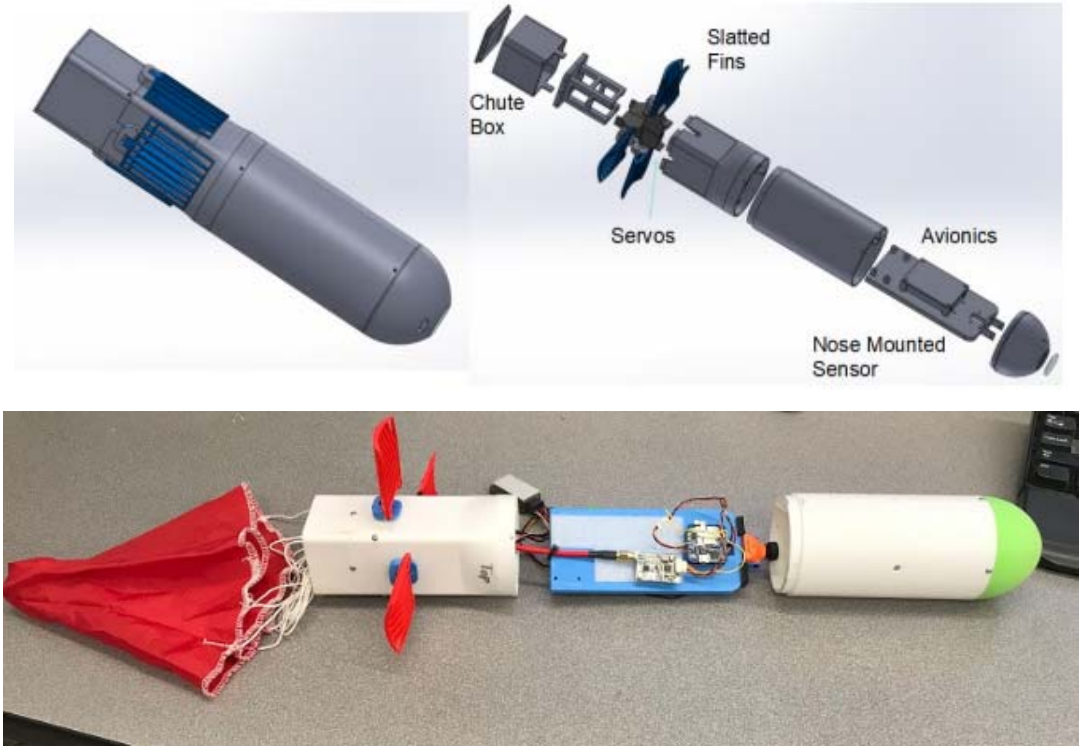

Figure 4. Guided munition prototype designed by Robert Wright.

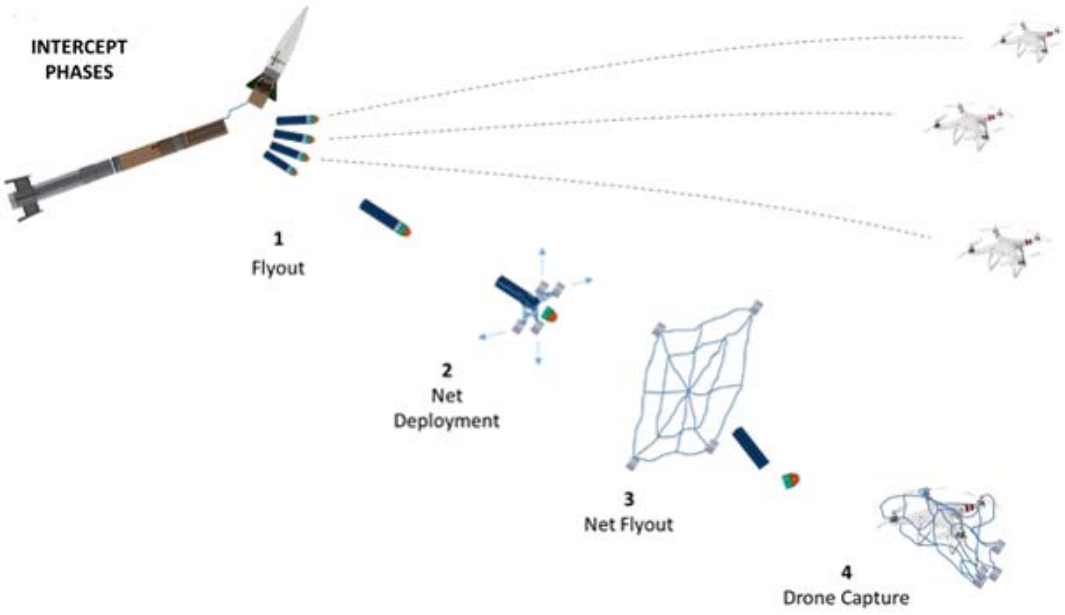

Figure 5. GM intercept concept of operations. Source: [15].

The overall SUAVE mission was designed around combatting threats similar to the Chinese UAV swarms mentioned above in Chapter 1. Sec. A. Background. The threats were specified as low-cost fixed-wing UAVs as described by Captain Kai Grohe:

> The small UAV considered is a fixed-wing vehicle intended to leverage technology developed for the hobbyist small aircraft market. This vehicle is described in some literature as a drone, but is not to be confused with a rotary wing aircraft, which relies on propeller thrust continuously directed toward the ground to maintain an altitude. [14]

The threats most similarly represent the fixed-wing swarm UAVs designed by the NPS consortium for robotics and unmanned systems education and research (CRUSER). The CRUSER project employs over 100 fixed-wing and 20 quadrotor UAVs that can be directed to perform coordinated aerobatic maneuvers and participate in dogfights with other drone swarms [16].

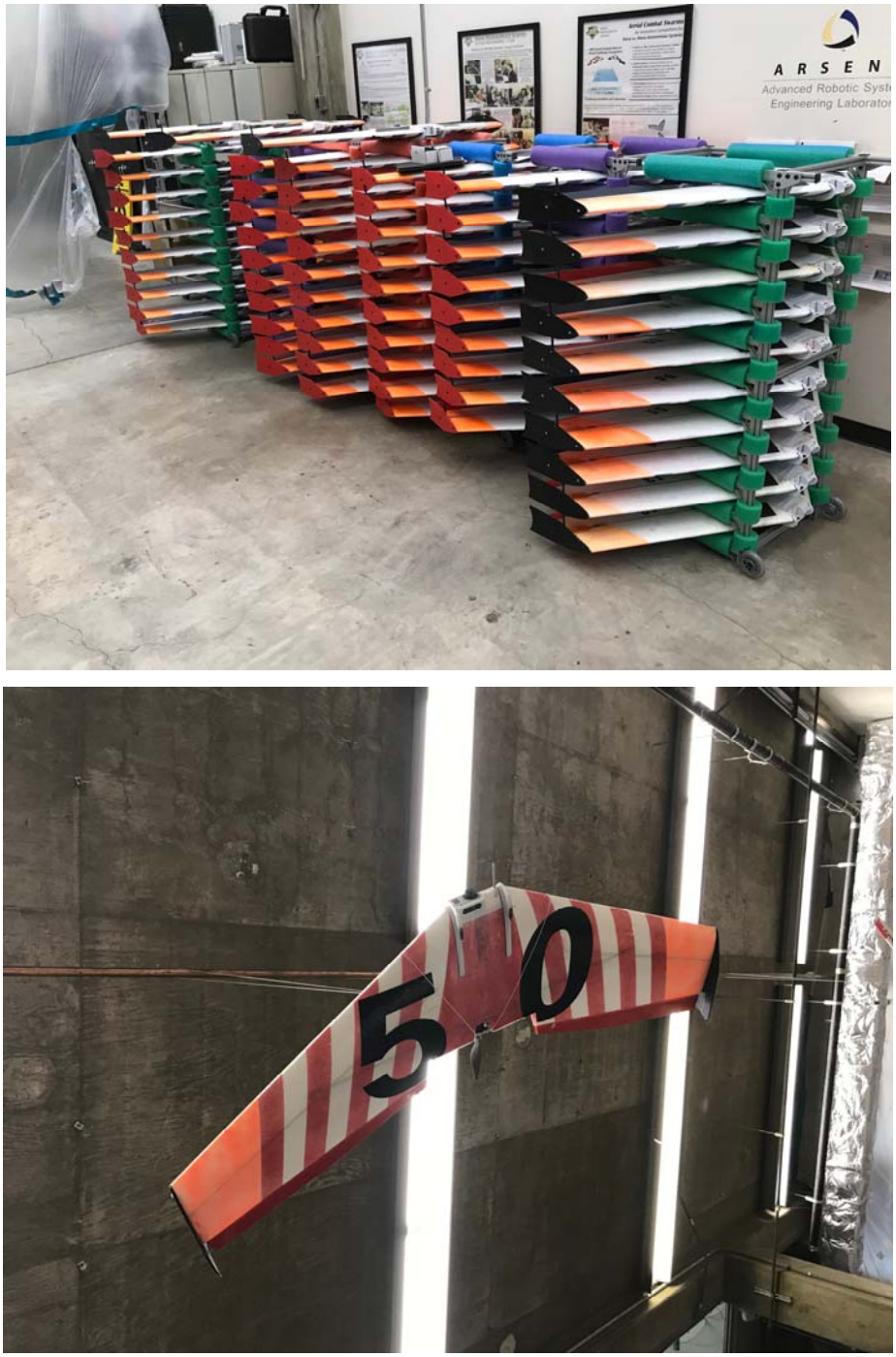

Figure 6. NPS CRUSER low-cost UAV swarm located in CAVR Laboratory.

Each UAV has a unit cost of $300, and their present capabilities coupled with potential weaponized variants make the CRUSER swarm vehicles great research tools during the development of the SUAVE.

This author sought to further the capabilities of the SUAVE concept by designing the upper stage and focusing on GM deployment capabilities. Specific attention would first paid to the deployment procedure of one single GM; following proof of deployment and control, a four-GM deployment bay would be designed and implemented into the SUAVE architecture. Other areas of research would include the operating limits suitable for GM deployment through the use of Computational Fluid Dynamics (CFD) modeling during ejection, as well as targeting hub analysis with respect to FOV, stability, and GM acquisition following deployment. These steps fall in line with the overarching objectives of the work:

1. Prove deployment of one guided munition (GM) and remote guidance capability
2. Extend deployment capability from one to multiple GMs
3. Track GMs following deployment from SUAVE vehicle

This thesis design defines deployment capabilities for the SUAVE and allows future researchers to direct attention towards the mission profile characteristics of target sensing and GM guidance following deployment and prior to target neutralization. In keeping with the main objective of cost-symmetry, the author utilized only commercial-off-the-shelf (COTS) systems and materials made in-house at the RPL.

THIS PAGE INTENTIONALLY LEFT BLANK

II. SINGLE MUNITION DEPLOYMENT

The first phase of the development effort consisted of designing and constructing a delivery vehicle for one single guided munition in order to prove control of GM after deployment. Data and demonstrated control of the GM from successful single-deployment would be used as reference points as the vehicle was extended to house and deploy four guided munitions.

A. DESIGN

The delivery vehicle for the single GM deployment utilized the same lower stage as the SUAVE designed by Captain Grohe. The body of the rocket was a Public Missiles fiberglass wrapped phenolic airframe tubing measuring 0.19 m (7.5 in) internal diameter [15]. The solid rocket motor housed in the lower stage was a Cesaroni M1300, which produced an average thrust values of 1303 Newtons (293 pounds-force) and average flight altitudes around 1524 m (5000 ft) [17]. A coupler connected the lower stage and upper stage with shock cord so that upon parachute deployment, one A-parachute and one drogue safely brought the entire vehicle down in one piece. The upper stage consisted of similar fiberglass wrapped phenolic tubing connected to a tangent ogive nose cone.

Figure 7. SUAVE lower stage SolidWorks design by Captain Grohe.

The objective of the single munition deployment was mainly to prove control of the GM after deployment from the SUAVE vehicle. For this reason, the GM deployment mechanism was less of a design focus, and merely a means to eject the GM from the rocket body. Previous attempts to launch a GM inside the rocket body led to overheating of the internal electronics of the GM while on the launch pad. This was due to the complexity of design which required the GM to sit in the vehicle up to one hour before launch. A solution to this cooling problem was achieved by longitudinally deploying the GM out of the nose cone; the GM was simply slid into the nose cone 10 minutes prior to launch, and electronics were able to be air-cooled due to GM protrusion of 128.6 mm (5.06 in) from the vehicle body.

Figure 8. Single GM deployment from nose cone.

The initial GM deployment design consisted of a black powder charge triggered by a Perfect Flight StratoLoggerCF altimeter that would actuate a piston at apogee. The piston was 3-D printed in-house with a concave lower surface to create space for the black powder charge, and was expected to push the GM out of the nose cone at the specified time. A model of the single deployment actuation is shown below in Figure 9.

.

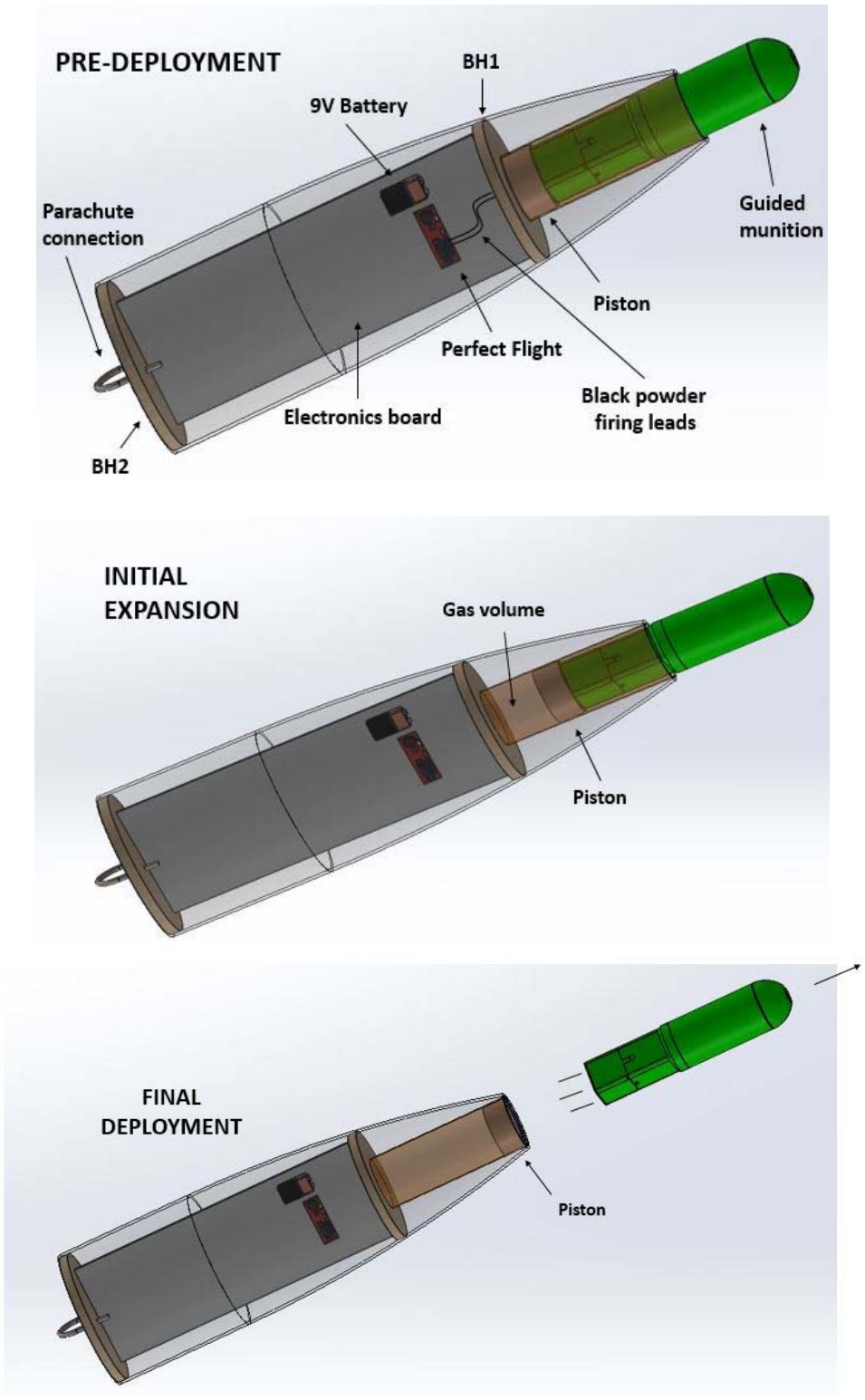

Figure 9. Stages of single GM deployment from nose cone.

Housing the GM in the nose cone was achieved by trimming the tip of the cone to an inner diameter of 77.72 mm (3.06 in), which matched with the outer diameter of phenolic tubing that the GM was designed to fit within. For the electronics to be adequately cooled, it was determined that 128.6 mm (5.06 in) was required to protrude from the rocket, leaving 179.45 mm (7.07 in) to be housed inside. The 32.77 mm (1.29 in) piston required the phenolic tubing to be cut to 212.34 mm (8.36 in) and attached to an epoxied wood bulkhead (BH-1) inside of the nose cone. The electronics required to ignite the black powder were installed on a sliding plastic bulkhead that followed rails down the length of the nose cone. The electronics board could be easily slid in and out of the nose cone for repairs if necessary, and was connected to a free wood bulkhead (BH-2) to separate the electronics from the parachute. Two 431.8 mm (17 in) all-thread rods distributed the parachute load from BH-2 to BH-1. An arm switch was also installed through the wall of the nose cone to increase safety on launch day; the black powder circuit could be armed immediately before launch as opposed to during vehicle construction hours before launch.

Figure 10. Sliding electronics tray in nose cone.

B. 17 NOVEMBER 2018 LAUNCH

The first launch for the SUAVE vehicle took place on Saturday, 17 November 2018, at the Friends of Amateur Rocketry (FAR) test facility near Randsburg, California.

Goals for the 17 November 2018 launch included successful launch and recovery of the SUAVE vehicle in addition to successful deployment and control of the GM from the nose cone. The SUAVE vehicle was successfully launched and recovered with no issue, however problems arose surrounding the GM deployment phase of flight. The GM was prematurely ejected from the nose cone, and although video feed from the GM camera was transmitted, there was no control during descent. The GM failed to deploy its parachute and crashed into the ground.

Upon further investigation, the cameras from both the SUAVE vehicle and GM revealed the failure that had occurred. The control volume that housed the black powder charge in between the piston and BH-1 contained trapped air at ground-level atmospheric conditions. As the rocket ascended and atmospheric pressure dropped, the trapped air in the control volume expanded in attempts to equalize pressure to ambient. The atmospheric pressures at both ground and apogee were calculated using the barometric formula,

$$P = P_0 * e^{\left(\frac{-M*g*h}{T_0*R}\right)} \quad \text{Equation 1}$$

and the altitudes upon launch and apogee, respectively. The constant variables used in Equation 1 are shown in Table 1.

Table 1. Barometric formula constants. Source: [18]

Symbol	Parameter	Value	Unit
P_0	Average Pressure at Sea Level	101.325	kPa
M	Molar mass of dry air	0.02896	kg/mol
g	Gravitational Acceleration	9.80665	m/s^2
T_0	Standard Temperature at Sea Level	288.15	K
R	Universal gas constant	8.314	(N*m)/(mol*K)

The altitude above sea level at launch of 504.4 m (1655 ft) MSL corresponded to an atmospheric pressure of 95.44 Pascal (13.84 pounds per square inch), and the apogee

altitude from the Perfect Flight data altitude of 1665.7 m (5465 ft) similarly corresponded to a pressure of 83.17 Pa (12.06 psi). The resulting change in pressure (delta P) of 12.3 kPa (1.78 psi) caused a force of 79.53 N (17.88 lbf) to act on the bottom surface area (64.77 cm^2) of the piston. This internal force caused enough of the GM to be pushed out of the nose and the dynamic loading forces during rocket acceleration sheared the freestream-exposed surfaces of the GM in half. The upper half of the GM fell to the earth as shown in Figure 11 from the camera mounted on the SUAVE body, and the lower half initially remained in the nose of the rocket until the black powder charge triggered. The lower half of the GM contained the four fins used for aerodynamic control during free-fall and the GM parachute, which explains the lack of control authority during descent after the GM was sheared into two pieces.

Adequate deployment of a single GM was not verified during this test campaign, nor was successful controllability of the GM in flight. The lessons learned from this launch were analyzed and new measures were implemented into a redesigned model for the next launch in February 2019.

Figure 11. GM upper-half falling away, as seen by SUAVE vehicle.

Figure 12. GM lower-half remaining in nose cone, as seen by GM upper-half.

C. SINGLE DEPLOYMENT REDESIGN

The control volume between the piston and BH1 (refer to Figure 9: Initial expansion) was vented to ambient pressure 0.56 meters (22 inches) downstream of the GM leading edge in an attempt to equalize the pressure within the gas volume of the GM piston with the local atmospheric pressure. The location for this vent-hole was chosen because it was nearly the most aft spot on the nose cone in which a vent-hole could be installed before the rocket body began. This location assumed that the pressure outside the hole in would be similar to that of ambient, not affected by any flow separation coming around the ogive, and would ideally allow the pressure in the control volume to equalize with the atmosphere as the rocket increased altitude instead of applying force on the GM.

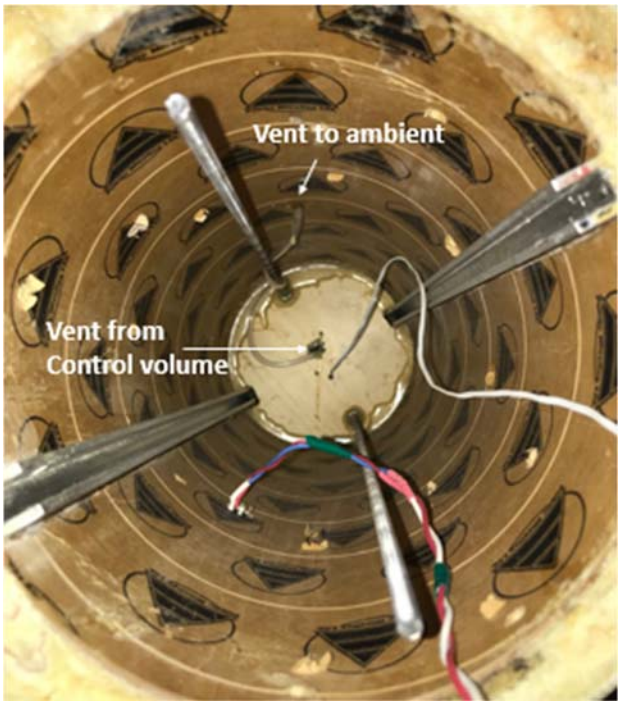

Figure 13. Installation of vent-hole from piston control volume to ambient.

To verify the vent-hole location as adequate for pressure equalization, CFD analysis was performed on the nose cone/GM profile at flight speeds. A model of the nose cone with GM protruding from tip was created and inserted into the CFD solver 'CFX' within the ANSYS Workbench suite. Another goal of the CFD modeling was to gain further insight into other reasons underlying why the GM prematurely deployed during the November 2018 launch. The pressure differential created by increasing altitude was logically anticipated, however a complete CFD solution could reveal dynamics within the boundary layer, especially near the connection of the nose cone and GM, which also contributed to the failure. One prediction was that the flow over the "step" between the nose cone and GM resulted in a low pressure region that created a suction force in the direction the GM was prematurely deployed.

To analyze the interaction in a computational domain, the profile of the nose cone first had to be built in SolidWorks. The exact curve of the nose cone used for the project was unknown, so exact specifications were unable to be pulled from internet sources. However, the shape was visually identified as a tangent ogive cone and an equation

describing the profile could be solved for mathematically. The calculations for the tangent ogive curve of the specific nose cone used are shown in Appendix A.

A GM length of 0.13 m (5.06 in) protruded from the nose cone tip, and was easily implemented into the model using the original GM SolidWorks file created by Robert Wright. The surrounding structure of the nose cone was drawn within a 0.41 m x 0.94 m computational region and revolved into a 20 degree wedge to approximate an axisymmetric profile for CFD modeling. The CFX solver was run with inlet conditions at 158.26 m/s, the maximum velocity recorded by the Perfect Flight during the launch, and ambient relative pressure at 0 Pa.

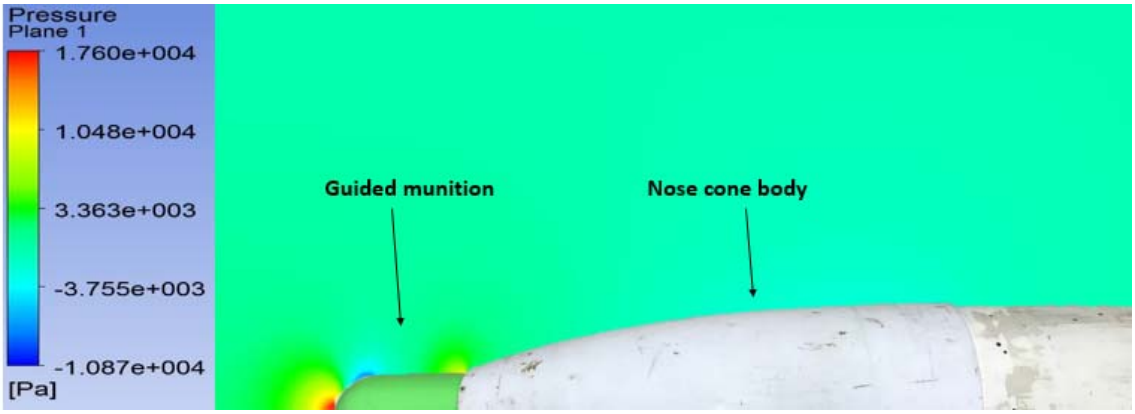

Figure 14. CFD global pressure solution of nose cone with GM protruding.

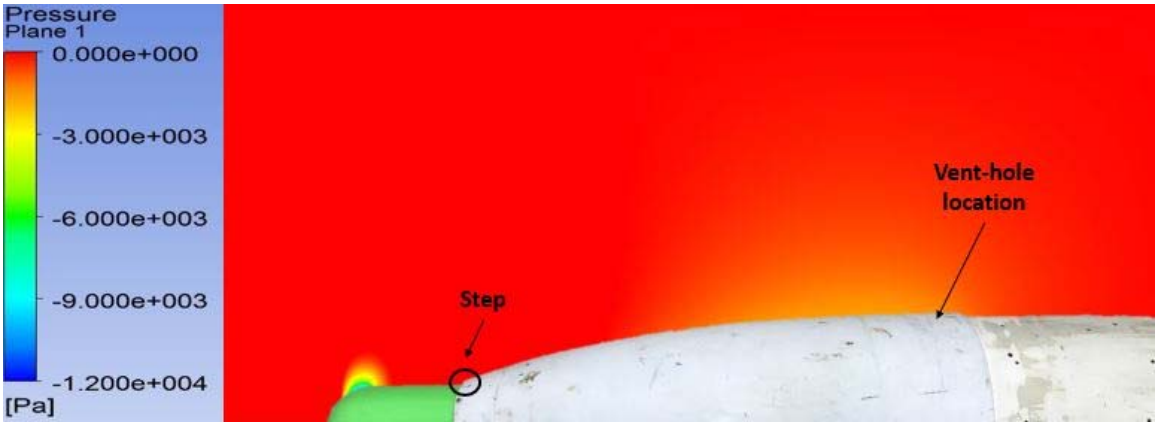

Figure 15. CFD relative pressure solution from -1.2e4 Pa to 0 Pa.

Two CFD solutions were plotted to show the global pressure solution, as well as only negative pressures. Since the ambient pressure was set to 0 Pa, all negative pressures indicate areas of lower pressure than ambient. The CFD solution shown in Figure 15 does not support the hypothesis that the step between the GM and the nose cone wall created lower pressure region. In fact, Figure 14 highlighted a pressure increase at the step.

Final enhancements were made to the SUAVE vehicle prior to the February 2019 including the replacement of the 3-D printed piston with a foam piston. This swap was made to provide an imperfect seal for the piston and eliminate the potential for the control volume pressure to eject the GM prematurely. The foam piston would allow the pressure to neutralize around the GM during flight, and with the addition of the vent-hole the chances for a successful ejection were increased. The nose cone phenolic tubing had been damaged during the November 2018 flight, and that was the last repair made to the vehicle.

Figure 16. Nose cone tubing damage and repair.

D. 23 FEBRUARY 2019 LAUNCH

The second launch took place at the FAR site on 23 February 2019. The goals for the launch were consistent with the November 2018 launch: successfully deploy one GM from the SUAVE vehicle and then prove control authority of GM once ejected. The new

measures accounting for pressure variations during flight proved to be adequate as both deployment and control authority of the GM were demonstrated. The SUAVE vehicle reached an apogee altitude of 1161.29 meters (3810 feet) AGL (above ground level) and maximum speed of 158.5 m/s (520 ft/s) from the Perfect Flight data:

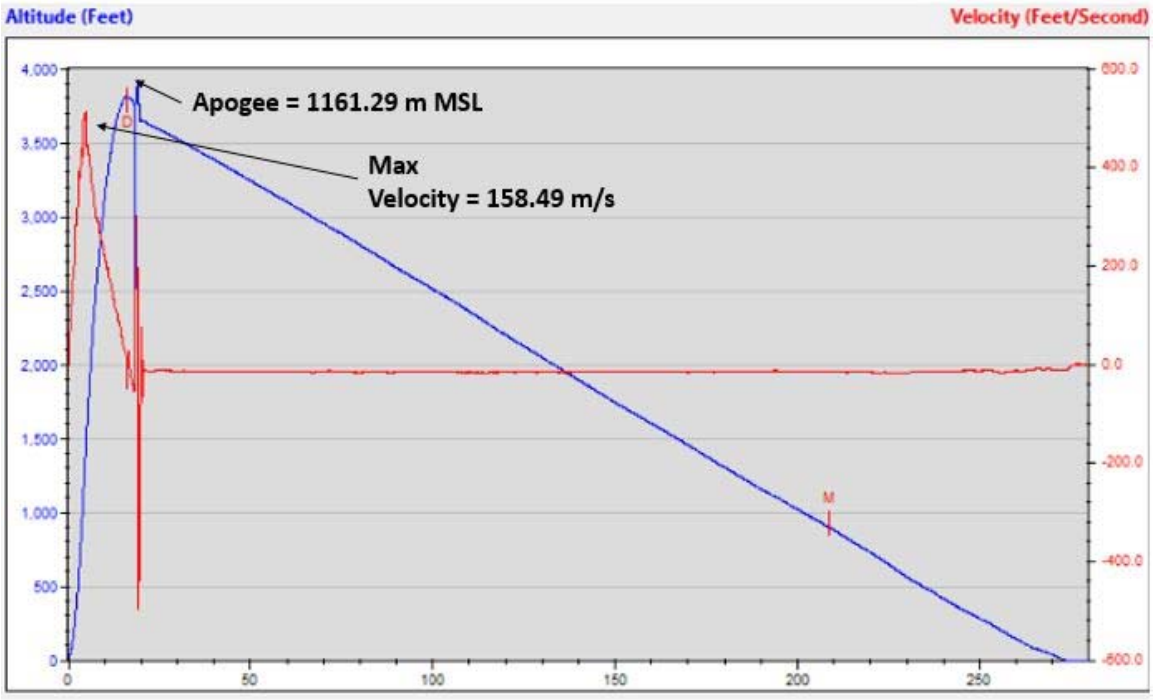

Figure 17. Perfect Flight data from SUAVE vehicle.

The main parachute deployed at 274.3 meters (900 feet) AGL, and the GM deployed promptly at apogee. The GM remained inside the nose cone until deployment, as shown by the GM maximum altitude of 1001.27 meters (3825 feet). Once ejected, Robert Wright used the camera on the GM nose to steer the payload via remote-control. A natural spin occurred immediately after deployment, but Wright was able to demonstrate control authority by slowing the spin rate to zero with a 15 degree counter spin command. The GM then overcorrected and began spinning in the opposite direction. Full control was not achieved due to a very high level of sensitivity, however the ability to eject a GM and control the fins from the ground was a building block upon which the SUAVE project will

build upon. In addition, the GM parachute deployed and landed smoothly which was a major improvement from the November 2018 launch. The safe recovery of the GM supported the mission of reusability for the SAUVE vehicle and GMs.

Figure 18. Impact from November 2018 test (Left) and successful recovery of February 2019 test (Right) results.

The major takeaway from the single GM deployment campaign was the necessity to account for even minor changing pressures within control volume cavities in the rocket body. The next step of deploying four GMs would be built upon the information learned in this launch; control volumes would be managed to ensure the same mistakes would not happen in the future, and the GMs would be moved inside the SUAVE body to prevent the possibility of premature ejection. The control authority demonstrated by Wright indicated that controlled munitions ejected from the SUAVE vehicle was possible, and would need to be built upon further to achieve GM stability.

III. MULTI-MUNITION DEPLOYMENT

A. BACKGROUND RESEARCH

1. GM Housing

Following the successful deployment of one GM from the SUAVE vehicle, the next step was to design and construct a deployment stage with multi-munition ejection capabilities. The 191 mm (7.5 inch) inner-diameter of the rocket body provided a limiting factor for the number of guided munitions able to be packed within the rocket body; only four 0.071 mm (2.8 inch) diameter GMs could fit properly without obstruction at their present dimensions as shown below in Figure 19. The GM sizing was based on the design made by Captain Lobo, RCAF, and Robert Wright, which proved to be an adequate sizing to contain all avionics, cameras, and kill mechanisms.

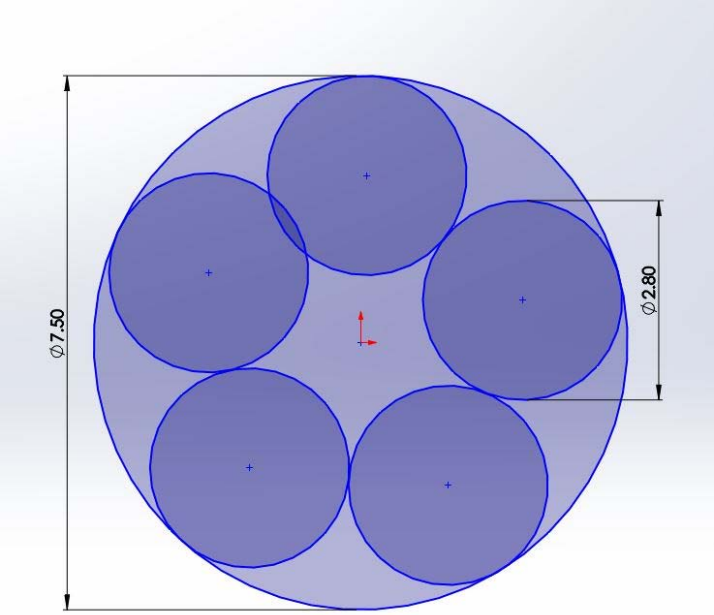

Figure 19. Five GM cross-sections within the rocket body.

As a result, four GMs were the maximum that would be attempted to be deployed out of the rocket body for the current design. Captain Grohe had experimented with a

gravity-assisted ejection of four GMs, where the GMs were housed upright in a bay. The GMs fell out of the vehicle during launch, and it was decided that they must be restricted in the longitudinal direction and rather deployed laterally. This decision was also supported by the single GM deployment results due to the undesired movement of the GM during launch. A laterally ejected GM would be bound on all sides: the top and bottom would be bound with one bulkhead each, and the walls of the rocket body would provide the lateral support to ensure an upright position. The GM bay was designed to house four GMs, each with 90 degrees separation to ensure an unobstructed departure during ejection. The bay was constructed with 0.076 mm (3 in) diameter phenolic tubing, one 191 mm (7.5 in) diameter wood bulkhead, and wood structural supports.

Figure 20. GM bay housing for four GMs.

2. Door Layout

A laterally ejected GM design would require doors that stayed rigid and shut during flight but opened upon command to release the GMs. Actuation would occur to open the

doors at the specified time. An additional actuation process would have to occur to eject the GMs from the bay following doors opening.

Military aircraft bomb bays were researched to determine the most effective method of housing munitions while still minimizing aerodynamic drag. Typically, military aircraft possess either semi-recessed or fully-recessed bay doors that consisted of two doors per bay that open from the middle of the bay outward [19].

Figure 21. Outward opening bomb bay doors on the Lockheed Martin F-35. Source: [20]

This type of bomb bay system minimizes the length of the door protruding into freestream during deployment and has been used on World War II bombers like the B-17 up to modern stealth aircraft like the F-35 and F-22. Efforts to further reduce protrusion and drag resulted in a few aircraft incorporating sliding bomb bay doors such as the RAF Blackburn Buccaneer [21]. One study from the University of Glasgow confirmed the use of sliding doors as advantageous over outward swinging doors due to the impact upon the pressure within the bay cavity following opening; the sliding doors took less time to reach open cavity steady pressure which had implications regarding lower drag values [22].

Sliding doors were decided to be too complex for implementation upon the low-cost SUAVE vehicle, especially since the rocket body shell was fiber glassed phenolic tubing that would not easily slide for multiple uses. In addition, four doors on a 191 mm

(7.5 in) diameter cylindrical surface are limited on space and would not be able to slide to one side without obstructing one of the other openings.

Outward opening doors were chosen and the two options considered were either one or two doors per cavity. Blowing the doors off and letting them fall alongside the GMs was not considered an option due to the potential hazards for the GMs and visibility of the nose cone, in addition to the necessity of reusability of the deployment vehicle as a main design point. This meant the doors would remain open after deployment and assist in the stability of the nose cone during descent. One study conducted by the U.S. Army Missile Command highlighted the rolling moment induced by wrap-around fins (WAFs), which most closely resemble a one door per cavity structure at certain angle of attack [23].

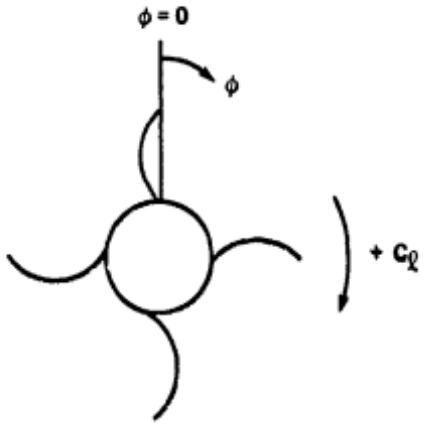

Figure 22. Rear view of wrap-around fins looking upstream. Source: [23]

The WAF architecture for the doors on the nose cone would be advantageous since the rolling moment would create spin-stabilization and keep the nose cone oriented straight downward. Spin stabilization induces an angular momentum vector that would be in this case pointed directly downwards and the roll rate would make the rocket

> sluggish in its rotational (pitch and yaw) behavior, allowing it to respond more nearly to the time average of disturbances than the individual disturbances themselves — and since the time average is generally much less than any one individual disturbance, this is greatly to the rocket's advantage. [24]

Spin stabilization impacts the altitude and velocity a rocket can reach due to the conversion of energy from translational (in direction of flight) to rotational, which results in lower flight velocities [25]. This would not present an issue for the nose cone application, as the doors would open after the nose cone was under canopy and descending to the ground. In fact, the longer time on station (time before reaching ground level) the more effective the final SUAVE vehicle design would be with regards to combatting enemy drone swarms. In addition, the nose cone would not be required to maneuver quickly and adjust trajectory to hit targets so the lack of agility from spin stabilization would be irrelevant.

The rolling moment from the WAF architecture could also be beneficial for the detection and resolution of both the GMs and the enemy drone swarms depending on the final target acquisition approach. The Rolling Airframe Missile (RAM) is an example of an airframe that uses a two-antenna interferometer that measures phase interference in one single plane; by continually rolling, the antennas are able to pick up energy from all planes [26]. The RAM is able to cut costs by only needing one seeker, and yet is extremely effective in resolving targets. The field of view (FOV) is also increased due to a slight off-center arc.

The deployment stage was chosen to have one door per cavity to take advantage of the capabilities that WAFs and an induced rolling moment potentially provide. For the first design, the doors were set at an angle of attack of 0 degrees, which would not induce a rolling moment, however depending upon flight tests regarding the stability of the nose cone during descent the doors could be slightly canted at an angle of attack to reflect the WAF characteristics.

B. GUIDED MUNITION (GM) BAY DESIGN

The doors retaining and protecting the GM units would have to remain closed until after apogee when the GMs were required to be deployed. This demand required a special actuation time that could be controlled either by the Perfect Flight altimeter through apogee detection or remote control from the ground. Servomechanisms (servos) were initially

considered, however one servo per door took up a large area within the GM bay and the increased number of moving mechanical parts which would likely increase the potential chance for failure. The most important part of the door actuation implies the ability to successfully keep the doors closed during flight, and therefore the servo would be continually requiring power to resist the doors from opening prematurely. Designs were shifted towards determining a way to have the doors remain passively closed at an unpowered state, and only require a power source once the doors were needed to open.

1. Electromagnet Analysis

Through an electromagnet approach, neodymium magnets on the doors would attract metallic objects within the GM bay, thus keeping the doors closed during flight. Since the magnetic force that would hold the doors closed would be natural, it would not require power during flight. In addition, the strength of the magnets used could be easily changed to meet the demands required during an especially turbulent launch and flight trajectory. To open the doors at the specified time, the attractive magnetic field would have to be negated by the magnetizing of an electromagnet to ensure the doors were pushed out to a certain distance.

The flow of electricity through a wire creates a magnetic field, which was discovered on accident by Danish scientist Hans Christian Oersted [27]. This groundbreaking discovery led to fundamental work by Andre-Marie Ampere, Michael Faraday, and James Clerk Maxwell, among others, to craft the branch of physics called electromagnetism. Wires can be wrapped around a ferromagnetic core made of iron or steel to increase the magnetic field strength once current is passed through the wire.

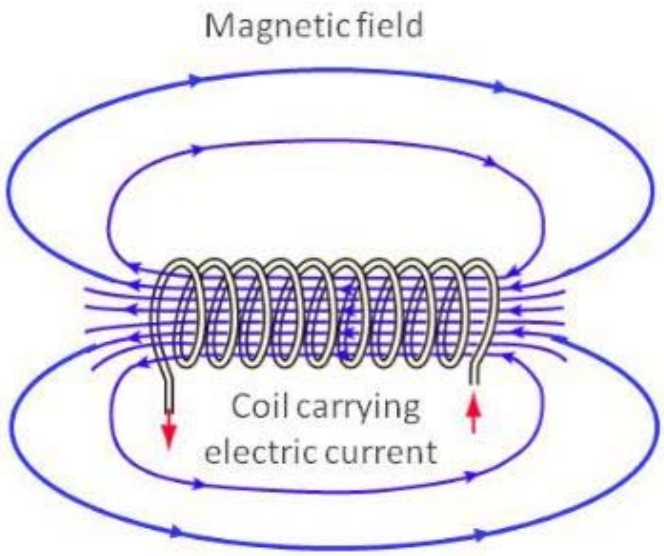

Figure 23. Magnetic field dipole created by current flowing through a coil.
Source: [28]

The benefit on this principle is that when the electromagnet is off, the magnetic domains within the iron/steel core point in random directions and negate any large magnetic fields [29]. It is not until current is passed through the wire that the magnetic domains in the iron core orient in the same direction as the magnetic field and add to the overall field strength. Once the current flow is stopped, the iron core loses magnetic alignment and the field disappears [30]. This phenomenon would be advantage for the GM bay door application since the magnets on the door would initially be attracted to the uncharged iron core. The core could be wrapped in such a way that once current was sent through the wires the iron core would magnetize and create a magnetic force strong enough to repel the attraction force from the door magnet.

A design was created using one electromagnet per door to hold the door during flight. A battery was attached to each electromagnet and was daisy-chained to the Perfect Flight altimeter. During the flight to apogee, neodymium magnets positioned on the door would attract the soft iron core of the electromagnet and keep the door closed. The nose cone would orient downwards after apogee and the Perfect Flight would connect the circuit of the battery and electromagnet. The wraps around the soft iron core would magnetize and

repel the neodymium magnet, allowing the doors to slightly open. The door hinges would be spring-loaded outward so that once the magnetic attraction was broken the doors would swing fully open. The GMs would be ejected using a carbon dioxide (CO_2) cartridge that would pressurize a control volume in the middle of the GM housing. Pressure relief holes drilled into the control volume would eject the GMs radially outward following CO_2 expansion.

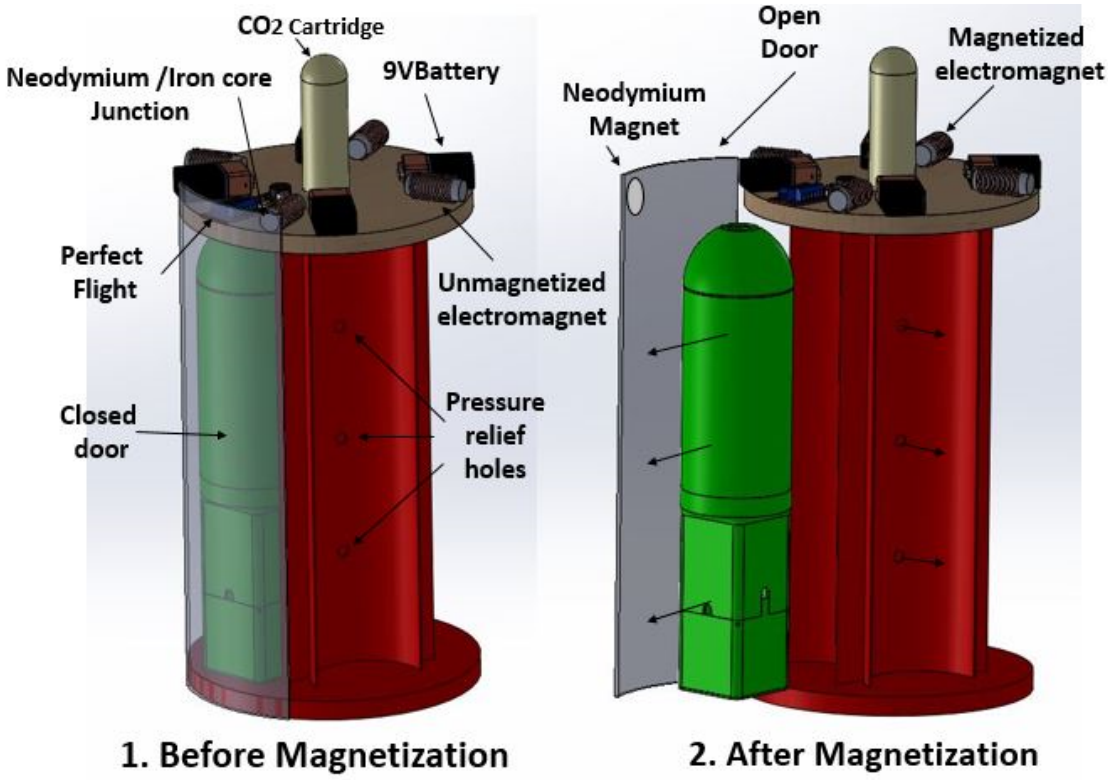

Figure 24. Door actuation and GM ejection stages using electromagnet actuation.

This design requires a magnetic field to be generated by the electromagnet that would be strong enough to overcome the attraction of the neodymium magnets. Calculations were performed to ensure the feasibility of this design, particularity with regards to the current flowing through the wire. It was assumed in calculations that no wraps would overlap each other, but be infinitesimally close without creating a short. The

governing equation that determined the magnetic field strength for a certain electromagnet was a derivation of Ampere's Force Law for the magnetic flux density, B, in Tesla [31]:

$$B = \mu * n * I \qquad \text{Equation 2}$$

The units of the intensity of a magnetic field, H, is Ampere per meter, however scientific practice and literature typically use the flux density, B, as the main descriptor of a magnetic field [30]. The μ variable in Equation 2 represents the magnetic permeability of the specific metal material used as a core in Tesla/ampere meter; μ relates H and B [30] mentioned above. The variable "I" represents the current flowing through the wire in amperes, and n represents the turn density of wire turns wrapped around the core in turns/meter. The relative magnetic permeability μ could be rewritten as

$$\mu = \mu_0 * k \qquad \text{Equation 3}$$

where μ_0 is the magnetic permeability of free space (4π x 10^{-7} Newton/Ampere^2) and k was the maximum relative permeability of the specific metal core that can be referenced in tables. The turn density, n, in Equation 2 can be rewritten as the number of turns divided by the length of the core metal in meters. Since the maximum number of turns can be expanded as the length of the core metal in meters divided by the diameter of the wire, the turn density n could be rewritten as

$$n = \frac{\#\,Turns}{L_{core}} = \frac{1}{d_{wire}} \qquad \text{Equation 4}$$

Combining Equations 2, 3, 4, and Ohm's Law yielded a new formula for calculation of the magnetic flux density, B:

$$B = \frac{(4\pi * 10^{-7}) * k * I}{d_{wire}} \qquad \text{Equation 5}$$

The goal was to design an electromagnet that had a high enough magnetic flux density to cancel out the attractive force of the neodymium magnet, and yet keep current flow under the maximum allowable current for a certain wire gauge. Higher than allowable current values would burn up the wire and potentially damage the SUAVE vehicle. The parameters able to be manipulated to potentially achieve this goal were as follows:

- The type of Neodymium magnet used for the door
- The dimensions and type of metal core used within the electromagnet
- The size of copper wire used within the electromagnet
- The voltage supplied by the battery

Equation 5 highlighted that a high relative permeability, k, and low neodymium magnet flux density would be desired to ensure the flux density, B, of the electromagnet would suitably negate the neodymium magnetic field. A soft iron core was selected since it possessed a dimensionless relative permeability of 5000, which was an order of magnitude higher than other common metals such as Carbon steel (k = 100) [32]. A neodymium magnet was selected as the door magnet since it would be stronger than conventional magnets on the ascent and hold the doors in securely, but the weakest would be desired to ensure successful repulsion from the electromagnet when necessary. The weakest Neodymium magnet on the market was the N35 which possessed a magnetic flux density of 0.3657 Tesla, so that was the magnet used for calculation [33]. The next parameter to analyze was the current, I, in amps which from Ohm's Law could be rewritten with new variables V and R representing the voltage of the electromagnetic circuit in volts and the resistance through the copper wire in Ohms, respectively:

$$I = \frac{V}{R} \qquad \text{Equation 6}$$

The resistance, R, through the wire can be rewritten as

$$R = \rho * \frac{l_{wire}}{a_{wire}} = \rho * L_{core} * \frac{(d_{core}+d_{wire})}{0.25 d_{wire}^3} \quad \text{Equation 7}$$

where ρ is given as the resistivity of copper, 1.68 x 10–^{8} Ohm-meter, and d_{core} represents the diameter of the soft iron core in meters [34]. The overall current in Equation 5 was desired to be minimized, which meant the voltage must be minimized and the resistance through the wire must be maximized. The battery chosen to power the electromagnet was the 4.2 V Lithium-Polymer battery (LiPo) since they are commonly used for remote control applications due to their low voltage and high amount of current able to be drawn [35]. This would ensure the battery would not be strained in the event of a high current draw.

From Equation 7, the length and diameter of the core were required to be maximized in order to minimize the resistance. Due to space constraints shown in Figure 24, the maximum length of the iron core was 3.5 inches and maximum diameter was 1 inch. These values were converted to meters for calculation purposes. The final parameter able to be manipulated was the diameter of the wire, which when minimized would maximize the resistance. Wire gauge diameters were evaluated from 40 AWG to 1 AWG and compared to their corresponding maximum allowable current value [36] to determine if any electromagnetic setup was possible. With all variables optimized to yield the minimum possible current, Equation 6 and Equation 7 were solved to yield actual current and magnetic flux density as wire diameter varied.

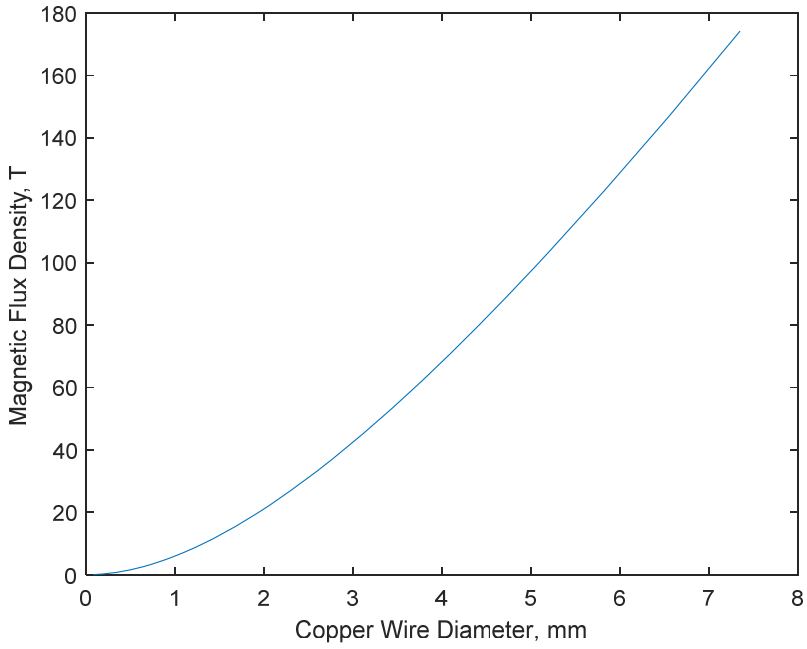

Figure 25. Magnetic flux density of electromagnetic configurations using 40 AWG (0.07 mm) to 1 AWG (7.35 in) copper wire.

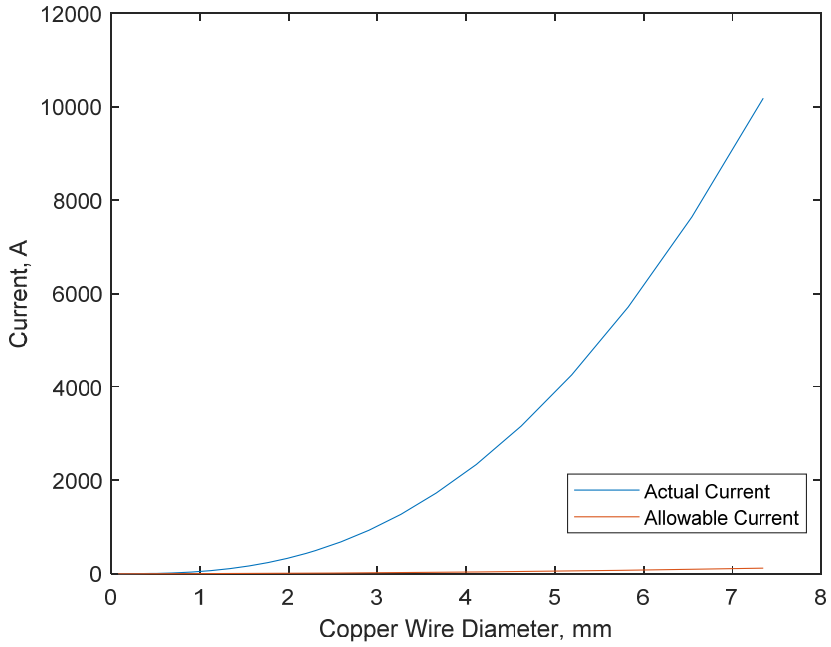

Figure 26. Actual current vs. allowable current for electromagnetic configurations using 40 AWG (0.07 mm) to 1 AWG (7.35 mm) copper wire.

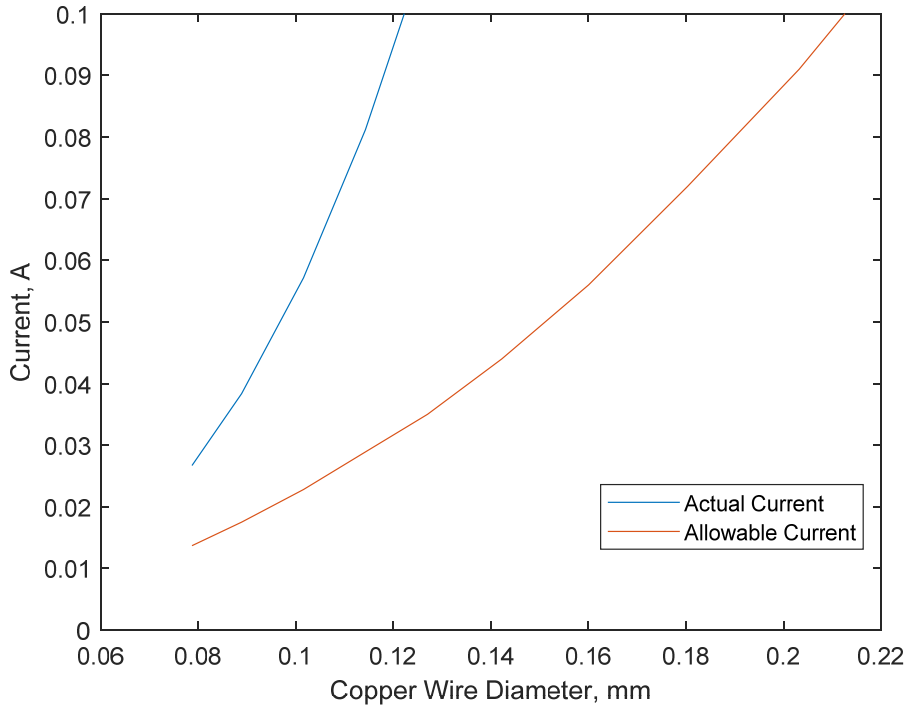

Figure 27. Figure 26 plot zoomed to endpoint.

Figure 25 highlighted that for any copper wire size, the resulting magnetic flux density would exceed the necessary 0.378 T to negate the magnetic field of the neodymium magnet and open the doors. The reason the flux values were so high was due to the high relative permeability of a soft iron core which majorly amplified the magnetic field. However, the feasibility of this design was disproved in Figure 26 and Figure 27 which showed the actual current values flowing through a certain electromagnet configuration compared to the maximum current limit a certain wire diameter could yield before melting insulation and failing. Using the optimized dimensions and electromagnetic components outlined above, no size diameter wire from 40 AWG (0.079 mm) to 1 AWG (7.35 mm) was able to withstand the current load that would be applied. As a result, using an electromagnet to deploy the doors was not considered a feasible endeavor. A new method of actuation for both the doors and GM ejection would have to be designed.

2. Mechanical Actuation

a. Design

Although the electromagnet design for actuation proved to be infeasible, the use of neodymium magnets to hold the doors closed was implemented into a new design. The new method was designed to require only one actuation to both open the doors and eject the GMs, eliminating the need for multiple batteries and a second form of actuation. A delay was required between door opening and GM ejection to ensure the GM did not make contact with the door; that lent itself to the idea of using a CO_2 cartridge and a sliding piston that would open the doors upon initial expansion of the CO_2 gas and after a specified time, the sliding piston would contact a bulkhead that would mechanically "kick" the GMs radially out. The neodymium magnets would still hold the doors closed during ascent, but rather than being attached to the door as in the first design, the magnets would be attached to legs connected to the sliding piston. Any movement of the piston would cause the magnets to become unaligned with metal squares on the door, thus freeing the door. The spring hinges mentioned in the first design would also be used in this design to fully open the doors following the movement of the piston. The piston was required to be 191 mm (7.5 in) in diameter to match the inner diameter of the phenolic tubing, and would house the neodymium magnets on the outward tip of each piston leg.

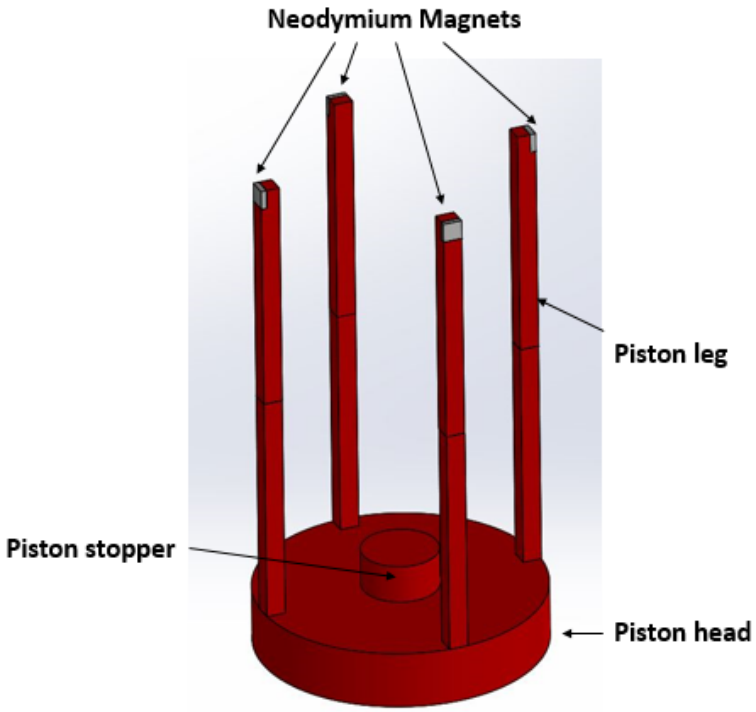

Figure 28. Piston design with legs and magnets attached.

The piston would then longitudinally slide down a cavity within the rocket body until it hit four "kickers." A piston stopper was installed on the inside of the piston head to ensure direct contact onto the kickers and to separate the piston from the kicker bulkhead. The kickers would be held in place with a dowel pin at their pivot point on the kicker bulkhead and were so designed to sweep out of the rocket body with their lower section following piston contact with their top section. The kicker bulkhead would have similar dimensions to a typical wood bulkhead except for the kicker openings and mounts, in addition to the openings to allow the piston legs to pivot.

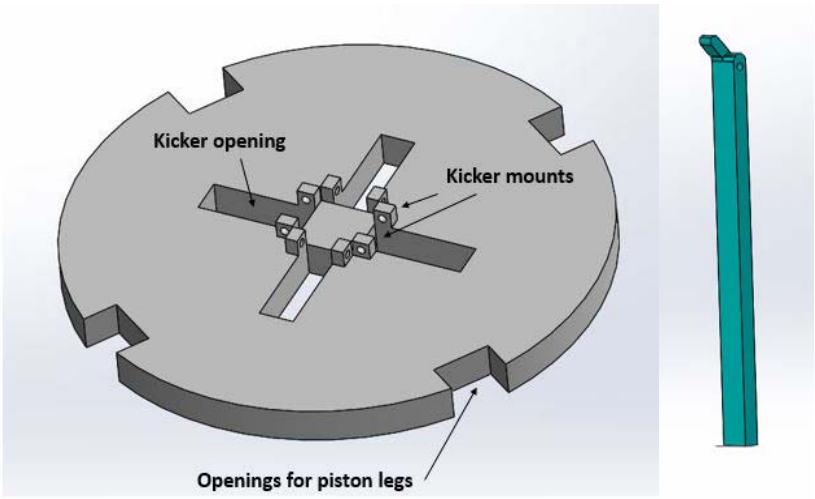

Figure 29. Kicker bulkhead (Left) and kicker (right).

Half of the top end of each kicker was removed to allow all four tops to lay flat after contact with the piston stopper, as shown in Figure 30. Slight modifications were made to the GM housing used in the first design; the pressure relief holes were removed and slots were cut so that the kickers could hang down and not contact the GMs while at rest.

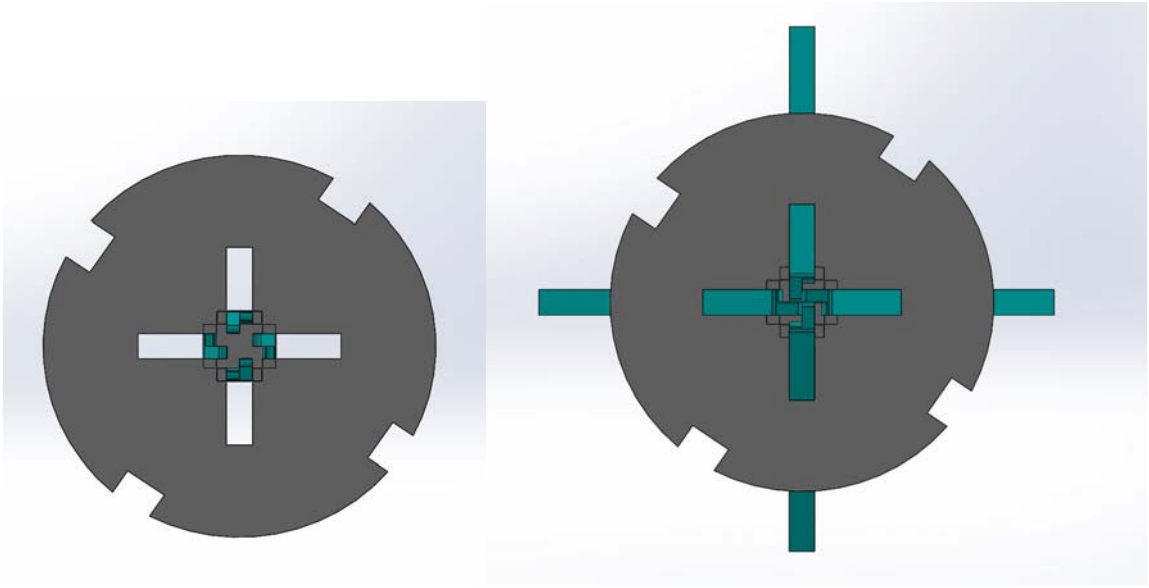

Figure 30. Kickers at rest (Left) and fully extended (Right).

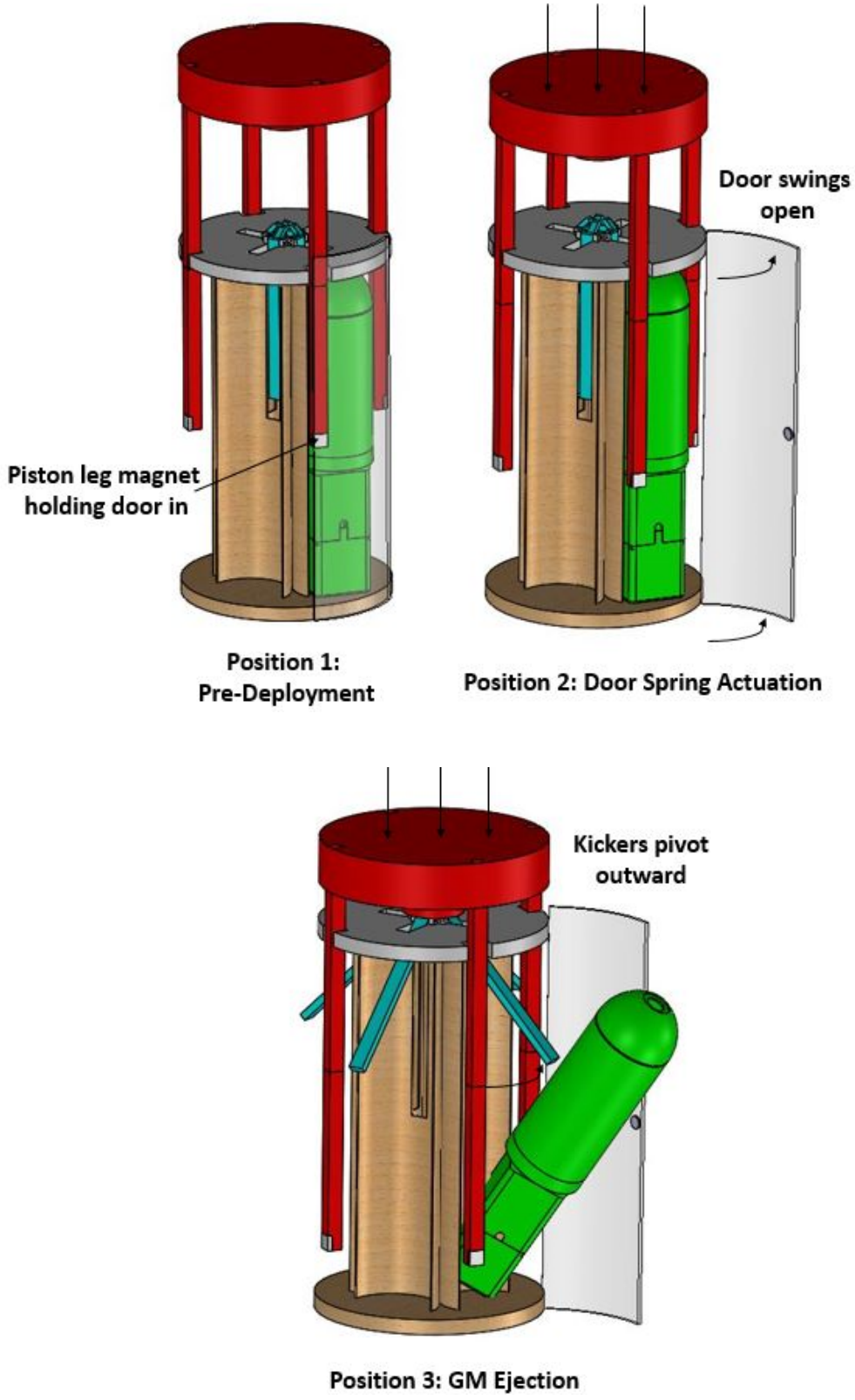

Figure 31. Mechanical GM ejection with piston.

The piston actuation would be contained within a 1.21 m (48 in) section of the rocket called the GM bay. 11.43 cm (4.50 in) separated the kicker bulkhead from the piston base to provide the delayed kicker response after the doors were opened. The CO_2 bulkhead sat another 11.28 cm (4.44 in) above the piston head to leave room for the CO_2 system and to create a control volume necessary for pressurization. Due to the high accelerations experienced at launch, it was determined that the piston would stand a greater probability of acceleration-based actuation if it was oriented legs-down on the launch pad. A legs-up orientation would allow the piston to remain in the same general position even during high g-loading, and once the GM bay/nose cone structure flipped over after apogee, the piston could use added assistance from gravity for actuation. In this configuration, however, the GMs would be deployed tail-first as opposed to nose first. CFD analysis was later performed to determine the performance of the tail-first deployment, however the entire GM bay was designed to be reversible in the event that a nose-first deployment was desired.

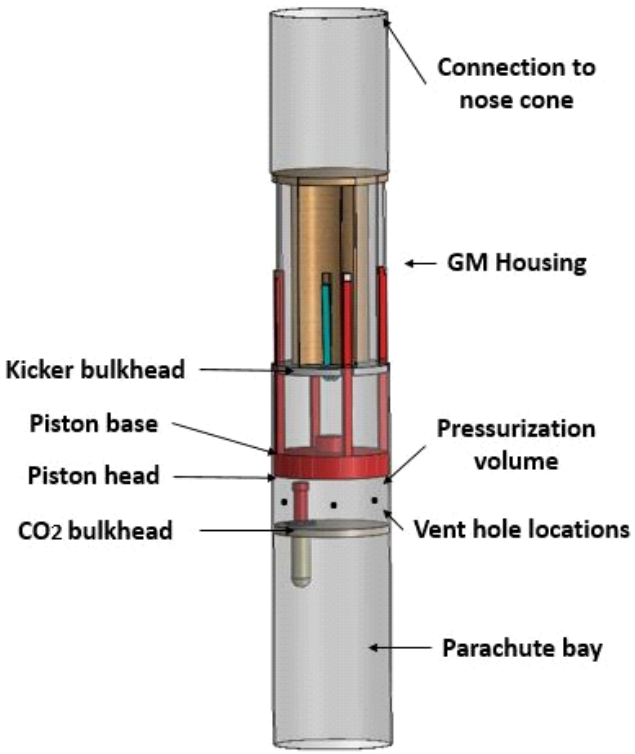

Figure 32. GM bay orientation on launch pad.

b. Construction

The design was developed into a full-scale functioning system. The piston with four piston legs, four kickers, and the kicker bulkhead were 3-D printed with the Ultimaker 3 machine with Polylacitc Acid (PLA) material. The GM housing modified a structure designed by Captain Grohe, and was glued to the kicker bulkhead. Four door openings were cut out from the main tubing, and door inserts were cut to size from extra tubing. The door sizing was determined by finding the arc length necessary to allow a GM to fall out of the rocket body without hitting the piston legs or door hinges. The green arc length at the top of Figure 33 included both the opening for a GM to fall out unobstructed and the piston leg cross-section; the arc angle of 57.4 degrees corresponded to an arc length of 95.5 mm (3.76 in). The doors were cut to this arc length in width and 34.29 cm (13.5 in) in length to fully cover each GM. Door holes were cut with 10.16 cm (4 in) arc lengths to allow for the door spring hinges to fit within the opening as well.

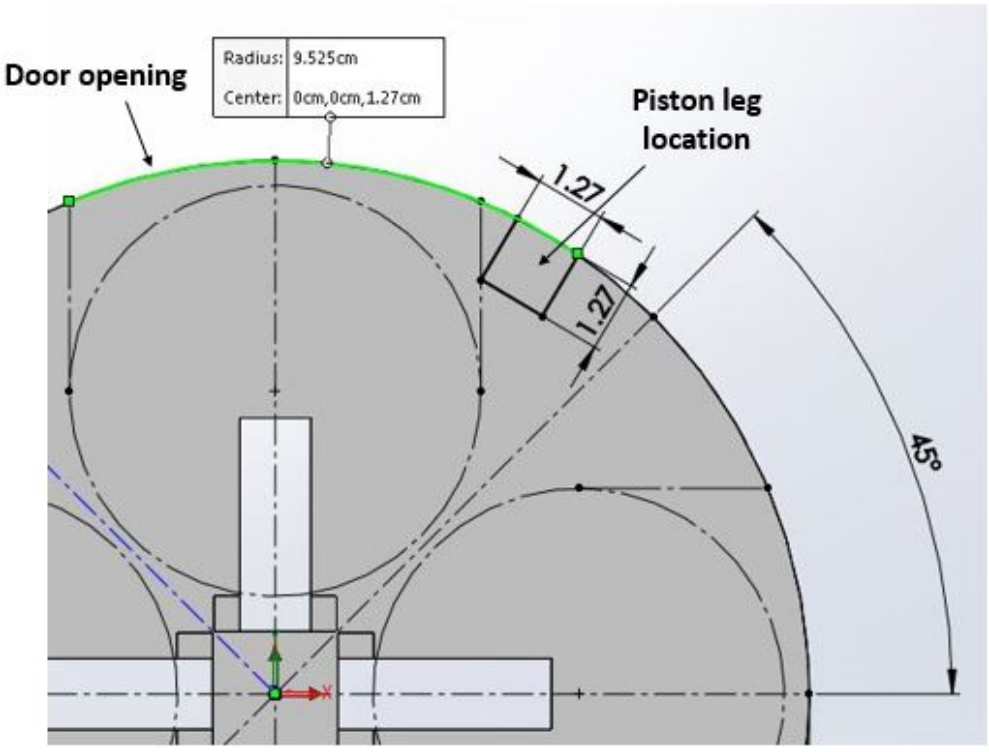

Figure 33. Kicker bulkhead sketch to determine the necessary door arc lengths.

Figure 34. GM bay full-scale model used for testing purposes.

All components including doors and hinges were implemented into the full-scale model to undergo several tests. The tests were designed to determine the necessary CO_2 and pressure relief hole sizing to ensure the piston would actuate when desired yet not break any components. The results from the sizing tests were used to develop the final GM bay to be used for flight; a final ground test validated that the flight model could perform adequate GM ejection.

C. GM BAY TESTING

1. Pressure Relief Hole Analysis

The importance of pressure relief holes for a rocket with closed control volumes was realized during the single munition deployment. The premature ejection of the GM due to pressure expansion with increasing altitude demonstrated that significant analysis would be necessary to ensure the same mistake was not repeated. The multi-munition deployment system relied on a similar pressurization chamber that could potentially create a pressure force on the piston head during ascent, and if that force exceeded the force necessary to actuate the piston the GMs would be ejected prematurely.

Pressure relief holes, also called static pressure port holes or vent-holes, are incorporated on nearly all developmental rockets of significant diameter due to the decreasing pressure of the atmosphere with altitude, as learned during the single munition launch. Smaller diameter rockets (less than 2–5 centimeters) do not have enough surface area on doors or bulkheads for the pressure difference between ground and at altitude to exert a significant force upon, however once surface areas are increased, these vent-holes are absolutely necessary. Highly sophisticated launch vehicles including the Space Shuttle utilized pressure relief holes; the holes were added within the cargo bay to ensure the cargo bay doors did not open due to differential pressure while ascending into orbit [37]. Pressure relief holes are also drilled for pressure equalization for correct altimeter readings, so each section containing Perfect Flight altimeters would need vent-holes as well. The location of the vent-holes is not of critical importance, however they must be oriented perpendicular to the freestream flow so that no air is forced into the rocket during flight [38]. The tests performed sought to determine the correct CO_2 cartridge and vent-hole sizing combination that would balance the two following characteristics:

- Relief holes large enough to equalize atmospheric pressure within control volume to eliminate unexpected door opening during ascent
- Relief holes small enough to guarantee actuation from CO_2 pressurization, but not too large which would vent out the CO_2 gas pressure too quickly

a. Weights test for actuation force determination

The first test was performed to determine the force necessary to actuate the piston. The results from this test were used to determine the CO_2 cartridge size and required vent-hole size. The test consisted of stacking known quantities of weight upon the piston when in rest position. The piston made a relatively tight seal with the phenolic tubing and was held in place by the closed door/piston leg magnet connection, so a certain weight threshold would be necessary to get the piston moving initially. The weights were pre-weighed and post-weighed to ensure accuracy, and they were added incrementally to attempt to pinpoint the actuation threshold.

Figure 35. Incrementally adding weights to piston head.

Table 2. Weight test results.

Test	Weight (kg)	Piston Result
1	12.26	Actuation
2	10.75	Actuation
3	9.94	Actuation
4	9.92	No movement

Actuation was defined to be when the piston moved slightly to open the doors; the piston would then slide down the chamber and contact the kicker bulkhead. Four tests were conducted, as shown in Table 2. Each test ended once the piston moved and slid down the tubing. The weights were removed and the piston was reset to the rest position, and a smaller amount of weight was incrementally added. Test 3 resulted in actuation after the addition of 9.94 kg, however Test 4 saw 9.92 kg added to the piston head with no movement. The force threshold for actuation was assumed to be approximately 9.93 kg, equivalent to 97.37 N (21.89 lbf). This force would have to be exceeded by the CO_2 system to ensure adequate actuation.

b. CO_2 cartridge size determination

The two potential CO_2 cartridge sizes utilized for rocket operations at the RPL are typically 25 gram or 32 gram units. The 25 gram unit was first analyzed using the Ideal gas law [39] to determine the resulting pressure upon the piston head given the initial chamber volume.

$$P * V = n * R * T \qquad \text{Equation 8}$$

The calculations assumed that the CO_2 from the cartridge was a perfect gas with only elastic collisions, and that the cartridge pressure instantaneously expanded to the chamber volume upon cartridge rupture. The calculation was also conducted assuming no pressure relief holes in the rocket body, and the pressurization chamber was the initial volume between the CO_2 bulkhead and the piston head at rest (Position 1 in Figure 31). The volume, V, was found by multiplying the height of the pressurization chamber (0.113 m) by the surface area of the piston head. The number of moles, n, was found by dividing the unit size, 25 grams, by the molecular weight of CO_2 (44.01 g/mol). The temperature, T, was calculated at the previous flight altitude of 1665.7 meters by interpolating the Standard Atmosphere chart found in [39]. R represented the universal gas constant.

Table 3. Parameters for ideal CO_2 pressure calculation.

Symbol	Parameter	Value	Unit
V	Volume of pressurization chamber	0.00321	m^3
n	Number of moles of CO_2	0.568	mol
T	Temperature at maximum altitude	277.32	K
R	Universal gas constant	8.314	(N*m)/(mol*K)

The parameters shown above in Table 3 were entered into Equation 8 and the CO_2 pressure in the chamber, P, was solved to be 407,572.413 Pascals. This pressure acting on the piston head resulted in a force of 11620.76 Newtons. In English units, 2612.45 lbf would act on the piston head at initial chamber pressurization. The calculated force was much greater than the necessary 97.37 N (21.89 lbf) calculated in III.C.1.a, so further analysis for the 38 gram CO_2 cartridge was disregarded. The 25 gram CO_2 cartridge would be used in the SUAVE vehicle, and vent-holes would be added for pressure equalization and to diminish the 11.62 kN (2612.45 lbf) acting on the piston to ensure reusability on future efforts.

c. Pressure Equalization determination

The pressure relief holes needed for the pressurization volume shown in Figure 32 would have to equalize with atmospheric pressure to prevent unexpected actuation of the piston and unwanted ejection. The surface area of the piston head was 285.03 cm^2 (44.18 in^2), and the pressure difference from apogee to ground was 12.27 kPa (1.78 psi); a resulting pressure force of 349.19 N (78.65 lbf) would act on the piston head during flight. Since it was determined that only 97.37 N (21.89 lbf) was necessary to actuate the piston, the mission would fail upon launch if no vent-holes were added. A strong estimate for pressure relief hole sizing based on experience was to use a 6.35 mm (0.25 in) diameter hole for every 1638.71 cm^3 (100 in^3) of the chamber volume [38].

The volume used for this analysis was assumed to be the final chamber volume once the piston made contact with the kicker bulkhead (Position 3 in Figure 31). The distance from the piston head to the CO_2 bulkhead at this position was 19.35 cm (7.63 in); this position was chosen since it provided a worst case measurement for unintentional actuation. The final chamber volume at Position 3 was 5520.15 cm^3 (336.86 in^3) which indicated four 6.35 mm (0.25 in) vent-holes were necessary following the rule of thumb from [40]. An actual test using this final chamber volume was performed to empirically determine the pressure drop as vent-holes were added; however four 6.35 mm (0.25 in) vent-holes would be referenced as the necessary threshold to prevent unintentional ejection due to changes in atmospheric pressure.

Similar analyses were performed for the two other compartments that contained the Perfect Flight altimeters; two 3.18 mm (0.125 in) vent-holes were determined to be adequate for these volumes.

d. Pressure profile vs. vent-hole area study

An experiment was designed to record the pressure profile within the final chamber volume (piston at Position 3) as pressure relief holes were increased in size and number. The purpose of this analysis was to characterize how the maximum chamber pressure changed as the area of vent-holes were increased; this would validate the assumption made in III.C.1.c that four 6.35 mm (0.25 in) vent-holes would be adequate for atmospheric venting. Additionally, the pressure force acting on the piston needed to be dropped from 11.62 kN (2612.45 lbf) in order to protect the structural integrity of the 3-D printed components, so by adding vent-holes and watching the pressure drop, a certain vent-hole configuration could be chosen once the pressure force is significantly lowered.

The experiment was performed using a mock-up of the final chamber volume; this allowed vent-holes to be added with no real effect on the actual GM bay model. Once a vent-hole configuration was tested and selected, the vent-holes would be drilled into the actual model. The final chamber volume was used for this analysis to track the maximum pressure at the end of the piston stroke to ensure that the piston would impact the kicker bulkhead. The mock-up model consisted of a 19.38 cm (7.63 in) tall volume chamber

within a 191 mm (7.5 in) diameter phenolic tube with the actual flight CO_2 bulkhead attached to the top. The CO_2 bulkhead was outfitted with one 25 gram CO_2 system and a Swagelok fitting for a pressure transducer connection.

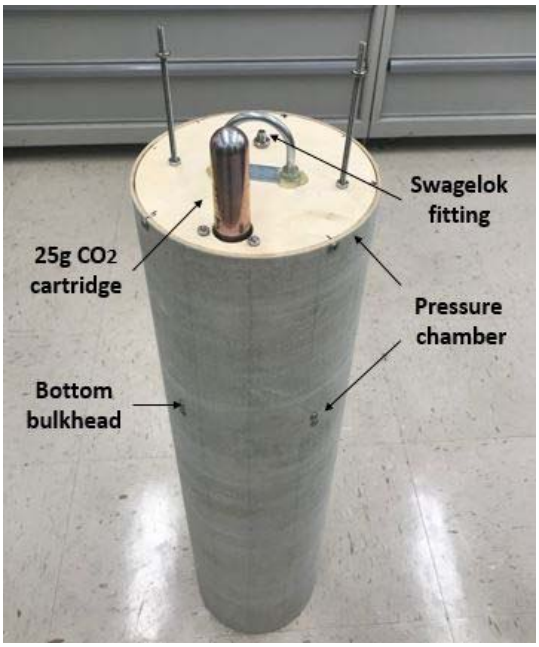

Figure 36. Mock-up model for pressure drop experiments.

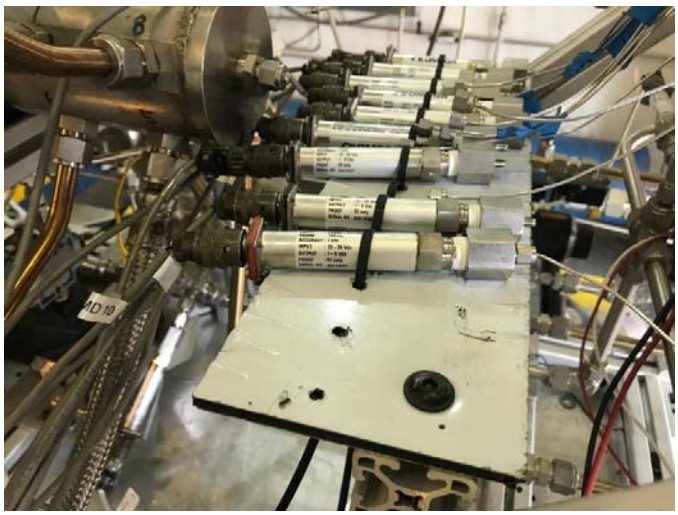

Figure 37. Pressure transducers from RDE test cell.

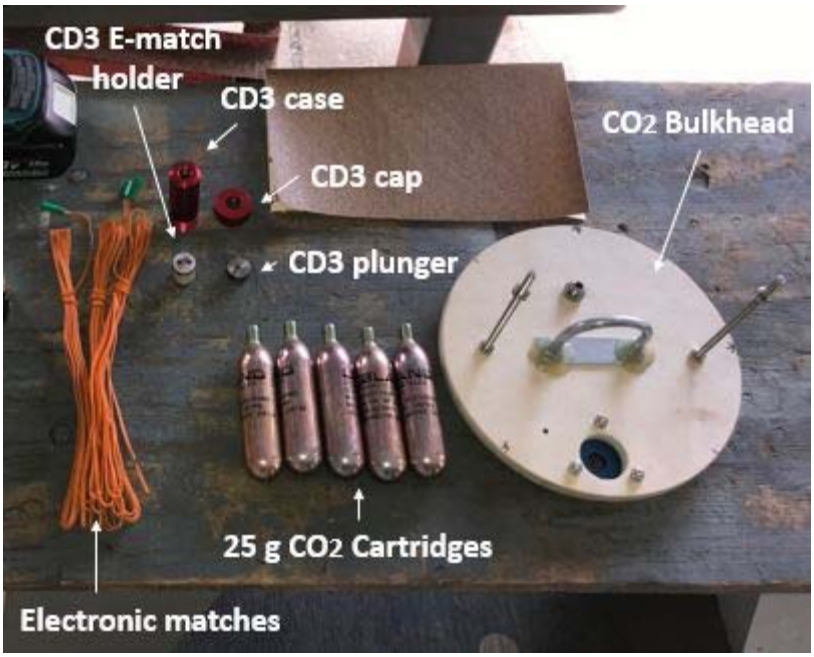

Figure 38. Materials used during pressure drop experiment.

The experiment consisted of blowing several 25 gram CO_2 cartridges into the pressure chamber with different vent-hole configurations. The system used to rupture the CO_2 cartridge was the Apogee CD3 unit, which relied on an electronic match (e-match) to ignite black powder inside of a sharp-tipped plunger. The plunger was the first material to be slid into the CD3 case; the e-matches were fed into an e-match holder which was greased with vacuum grease and slid into the CD3 case following the plunger. The e-match was ignited by connecting the leads to the positive and negative terminals of a 9V battery, thus creating a voltage difference and causing current to flow through a bridge wire. Resistive heating in the bridge wire exceeded the temperature required for the pyrotechnic initiator to ignite. The black powder then ignited and forced the plunger down the CD3 case until the sharp tip punctured the CO_2 cartridge. The CD3 system was connected to the cartridge through the bulkhead as shown in Figure 39. A pressure transducer from the RPL's rotating detonation engine (RDE) test rig was attached to the Swagelok fitting on the CO_2 bulkhead for voltage readings from the chamber during rupture. The voltages represented pressure values on the following scale: the 3.079V baseline to 5V represented an increase of 103.42 kPa (15 psig). All voltages were converted to pressures and were plotted during CO_2

expansion. The four vent-hole configurations and resulting maximum pressures and forces are shown in Table 4.

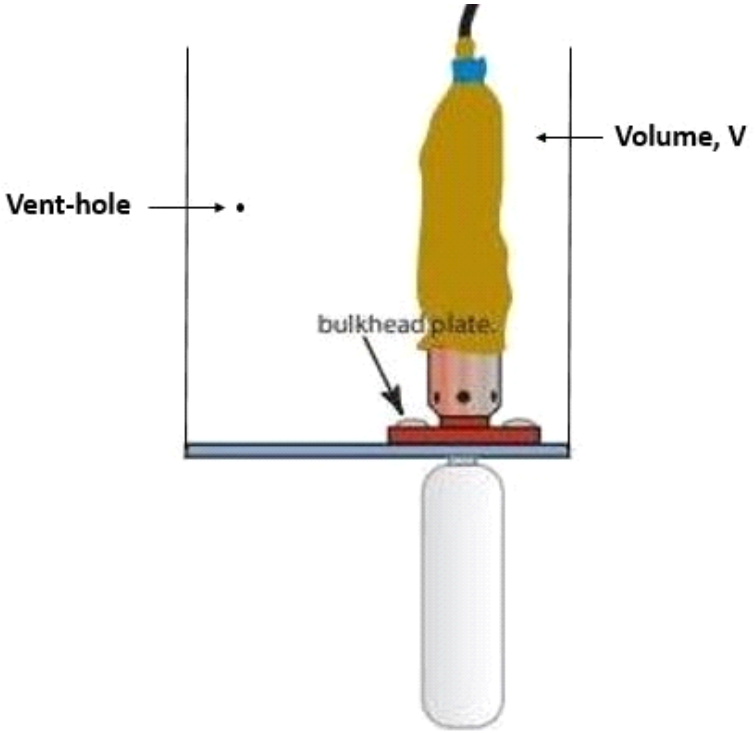

Figure 39. CD3 system with CO_2 connection. Source: [40].

Table 4. Pressure relief vent-hole configurations and results.

Configuration	Description	Total Area (cm^2)	Maximum Pressure (kPa)	Force (N)
1	Two 3.18 cm vent-holes	0.158	38.06	1084.79
2	Two 4.76 mm vent-holes	0.356	33.72	960.95
3	Two 6.35 mm vent-holes	0.633	30.47	868.60
4	Four 6.35 mm vent-holes	1.267	23.86	679.96

The first configuration of two 3.18 cm (0.125 in) vent-holes was arbitrarily selected as a baseline to begin the tests since the vent-hole area of 15.83 mm^2 (0.02454 in^2) was relatively small yet greater than zero. The test yielded a maximum pressure in the volume of 38.06 kPa (5.52 psig), which corresponded to a force of 1084.79 N (243.87 lbf) acting on the piston head. This force value was significantly lower than the theoretical value calculated in III.C.1.b, highlighting the impact vent-holes and increased control volume (from piston Position 1 to Position 3) had on pressure forces.

To determine a correlation between the vent-hole area and resulting pressure force, the vent-holes were each enlarged to 4.76 mm (0.1875 in) in diameter. The new effective vent-hole area was increased by 2.25 from configuration 1 to configuration 2, and the force upon the piston head was decreased to 960.95 N (216.03 lbf). In the third configuration, the holes were enlarged to 6.35 mm (0.25 in) and the pressure force was further decreased to 868.60 N (195.27 lbf). Two additional 6.35 mm (0.25 in) vent-holes were drilled for configuration 4; the total area ratio between configuration 4 and configuration 1 was 8:1, and the maximum pressure force in the chamber was dropped to 680.4 N (152.86 lbf).

The pressure within the experimental cavity during the four tests is shown below in Figure 41. Each increase in vent-hole area dropped the pressure curve as expected, and Figure 42 highlighted how the maximum gauge pressure decreased nearly linearly with increasing vent area.

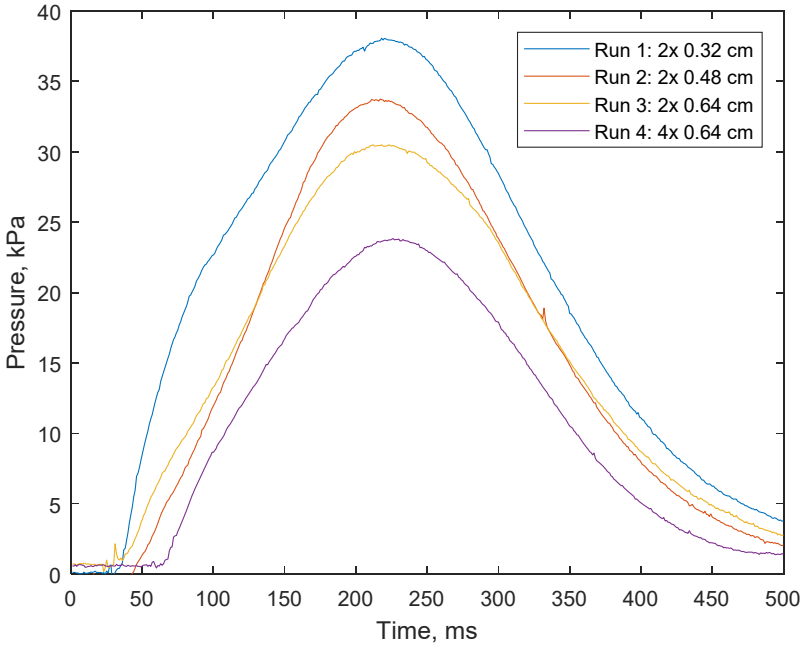

Figure 40. Pressure curves within control volume for multiple runs.

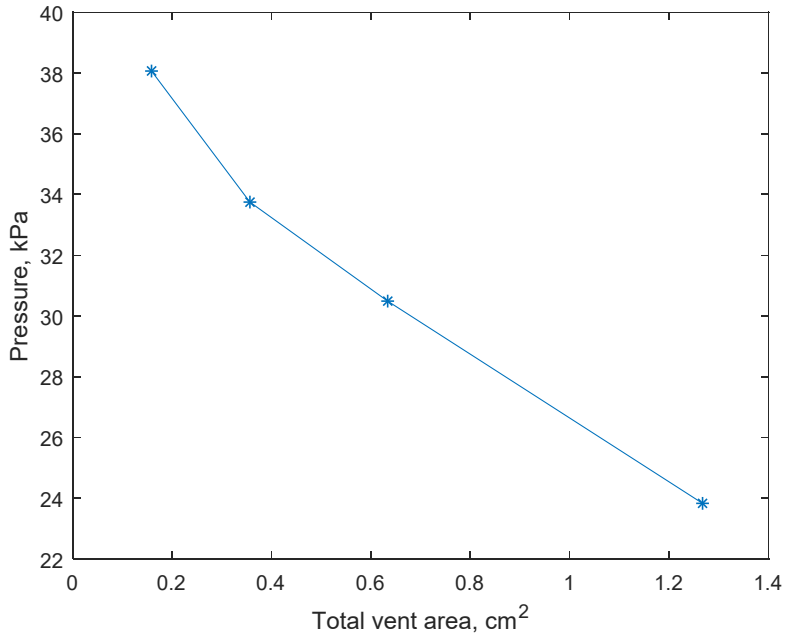

Figure 41. Maximum pressure within control volume vs. total vent area.

Configuration 4 was deemed adequate for usage with the flight system since 641.12 N (144.13 lbf) was greater than the necessary 97.4 N (21.898 lbf) to actuate the piston, yet not too severely high to risk damage of the 3-D printed PLA parts. Additionally, the force of 349.85 N (78.65 lbf) calculated in III.C.1.c that acted on the piston which would cause premature actuation due to the atmospheric pressure delta between ground and apogee altitude was proven to be adequately relieved; the force dropped 405.32 N (91.119 lbf) from configuration 1 to configuration 4 due to the addition of four 6.35 mm (0.25 in) vent-holes.

2. Ground Test for Flight Vehicle

Four 6.35 mm (0.25 in) vent-holes were added to the flight GM bay below the CO_2 bulkhead and above the piston head at initial position 1. A ground test firing of the CO_2 cartridge was conducted to verify the mechanics of ejection and to ensure that the four vent-hole configuration still resulted in actuation. Damage to mechanisms would also be checked upon conclusion of ground test.

The ground test was conducted in a similar manner to the vent-hole experiments. The CO_2 bulkhead was reinstalled into the GM bay 11.28 cm (4.44 in) above the piston head at position 1. The CD3 unit was rigged using the proper materials and connected to a 25 gram CO_2 cartridge. The vacant cavity in the e-match housing was plugged with another e-match to avoid black powder from escaping. The Swagelok fitting on the CO_2 bulkhead was again plugged into the RDE pressure data acquisition unit. The pressure readings within the control volume during expansion were not necessary for the test, however the fitting had to be sealed regardless and it was believed that analysis of the pressure data during piston movement could highlight issues with the design were the test to fail. A GM was inserted into one of the GM housing cavities with 5.08 cm (2 in) of foam pressing the GM tight to the kicker bulkhead.

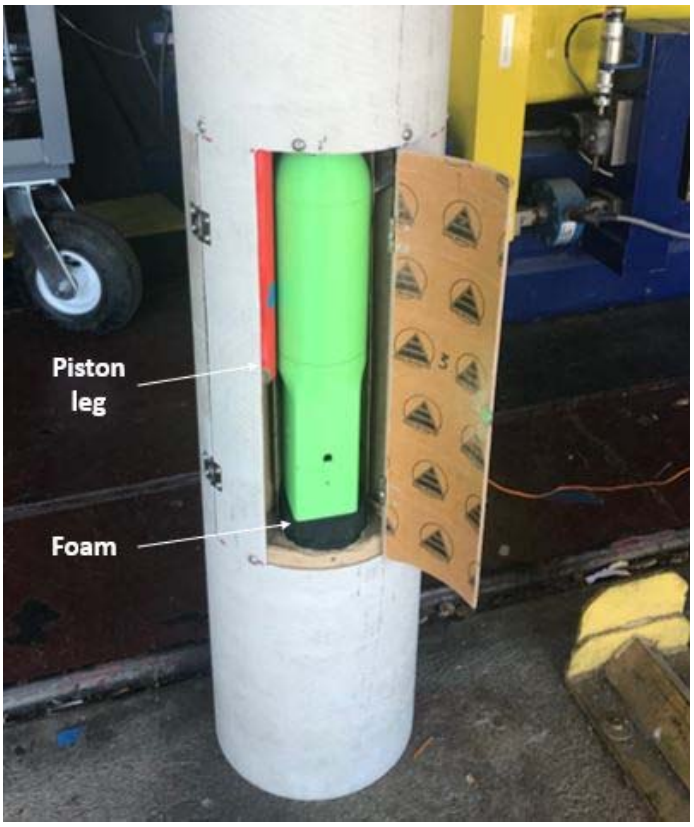

Figure 42. GM bay setup for first ground test.

CO_2 expansion was triggered using a 9V battery as before. The doors opened however the GM remained stuck in the housing cavity. Further inspection found that the foam underneath the GM was too thick and held the GM in place, restricting the kickers' ability to sweep outward. The foam was eliminated and the test rig was reassembled with a new CO_2 cartridge for the next test.

The GMs were successfully deployed from the GM bay during the second test; Figure 43 shows the progression from initial piston movement which opened the doors in frame 2 to the GM tumbling from the bay in frames 3 through 5.

Figure 43. GM deployment during ground test.

The GM bay components were inspected following the successful test to ensure both their durability and reusability. All parts were in satisfactory condition except for the piston stopper on the bottom face of the piston (Figure 28). The piston stopper was damaged by the kicker during the first test when the foam restricted the GM from moving; the kicker could not move outward and remained upright and punctured the piston stopper upon contact. The damaged PLA piston stopper is shown below in Figure 45 alongside the remedy: a machined aluminum disk epoxied onto the top of the stopper.

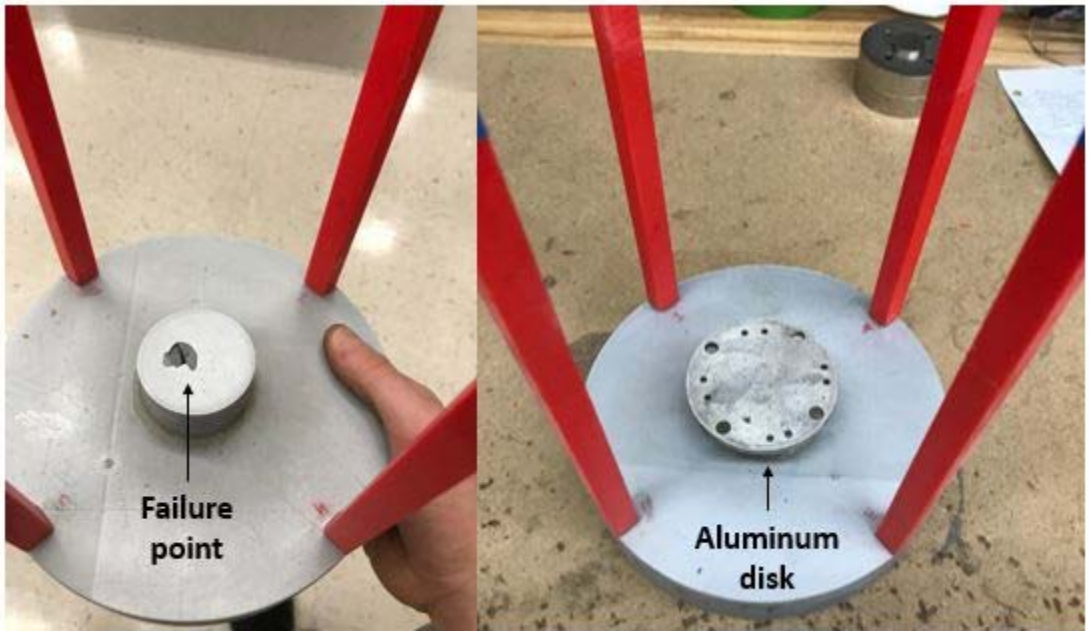

Figure 44. Damaged piston stopper (Left) and aluminum disk fix (Right).

The ground test validated the theoretical predictions for vent-hole sizing with regards to deployment. The four 6.35 mm (0.25 in) vent-holes adequately lowered the force on the piston to a manageable value to protect the components from damage, and yet did not vent out at too quick of a rate to negate the CO_2 expansion. Deployment using a piston and kickers was also validated, and would be ready for a dynamic flight test to verify the deployment mechanism at high subsonic speeds. Only during the full flight test would the vent-hole configuration be tested for atmospheric pressure equalization capabilities, thus concluding the vent-hole analysis for the GM bay.

Other takeaways from the ground test included the necessity to allow a slight amount of room in the housing cavity to ensure the GM does not get stuck, and the reality that the PLA components are survivable and reusable during a successful deployment, but could possibly fail in the event of a malfunction during flight.

3. CFD Analysis

The ground test proved the SUAVE vehicle's capability to eject munitions in a static environment while on the ground. Deploying GMs while traveling in forward flight at altitudes higher than 1000 meter would be a different environment that would bring additional challenges than on the ground. One potential problem identified was the possibility that GMs would be forced back into the GM bay following ejection due to the formation of the local flow field and possible recirculatory region near the bay cavity. Previous research in the literature supported the assertion that freestream flow over an open cavity results in a low-pressure recirculation region, which could possibly cause the GM to be pushed back into the cavity due to high pressure drag acting on the GM [41].

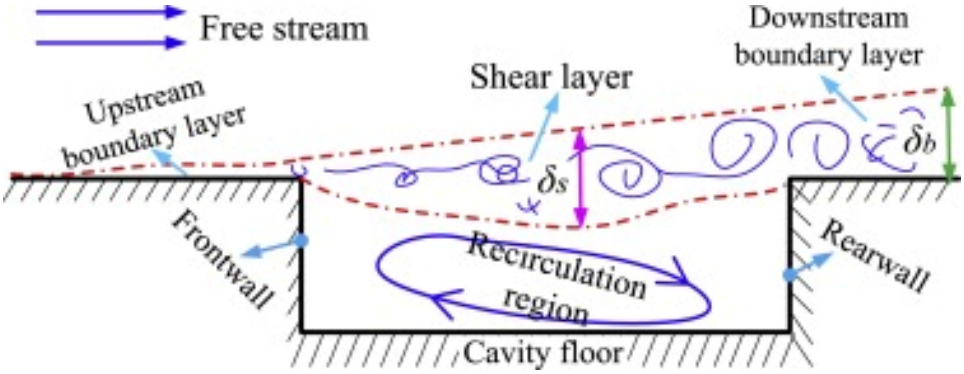

Figure 45. Schematic of recirculation region produced by free stream passing through an open cavity. Source: [41]

As mentioned previously, the orientation of the GM bay upon launch was restricted to keep the piston aft of the GM housing to prevent accidental piston movement upon the increased g loads when the booster was ignited, as shown in Figure 32. This implication required the GM to be ejected back-end first into the freestream as opposed to a nose-out approach. A nose-out approach is more aerodynamically conceptual, as it is similar to increasing the angle of attack of a body in a flow field; the pressures on the top and bottom faces of the body can be easily predicted. A back-end first ejection, the SUAVE vehicles method, was much more of an unknown action and would require modeling. The first test

done was to examine the flow over the open cavity after the doors opened, but prior to the ejection of the GM. This analysis would highlight complications that could potentially arise while initially pushing the GM into the freestream flow.

The ANSYS Workbench CFX solver was used for this analysis using an inlet flow of 6 m/s to match the estimated descent rate of the nose cone after stage separation. Turbulence modeling using k-epsilon transport equations was used to predict the turbulent flow characteristics due to the complex geometry of the model.

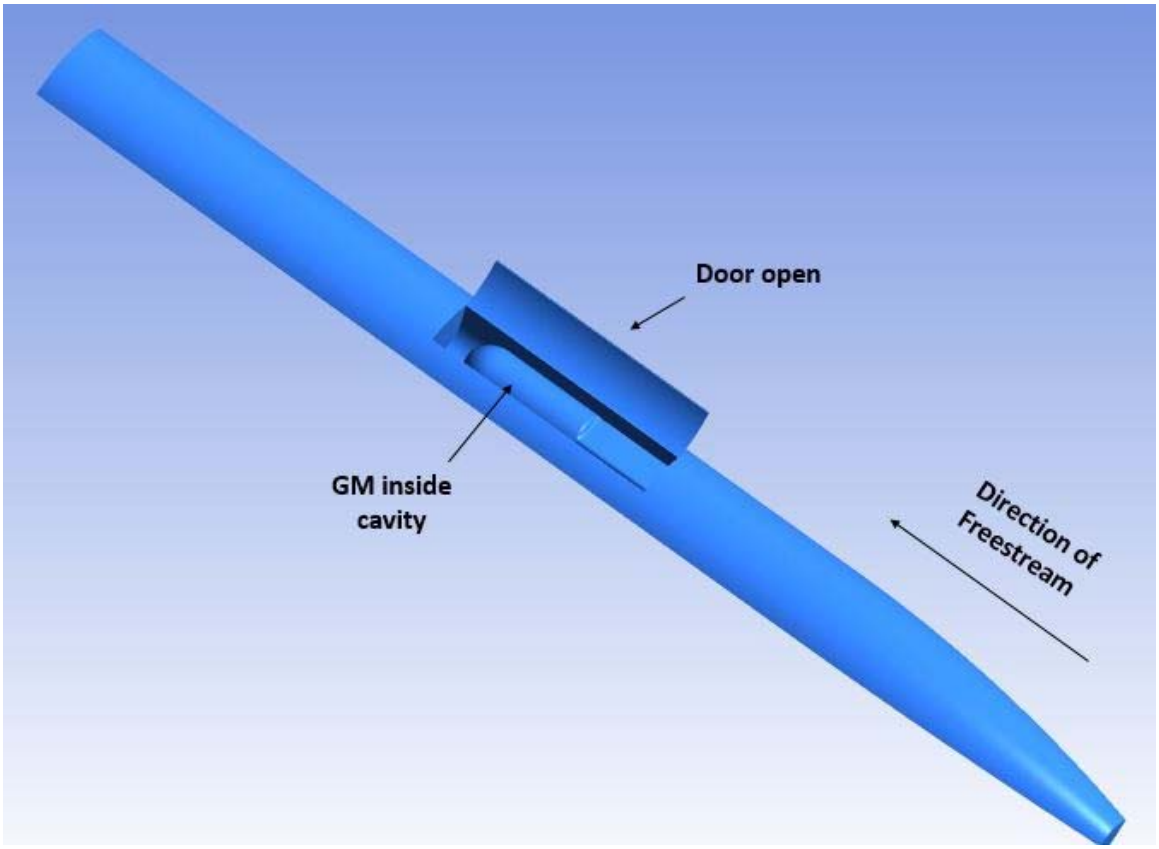

Figure 46. CFX Configuration 1: Doors open and GM inside cavity.

The flow over the cavity was relatively undisturbed by the presence of the doors, and although there existed a higher pressure region upon the upper surface of the GM, the

slow freestream velocity caused the pressure differentials to be minuscule. The GM would have no issue being pushed out of the cavity with the kickers.

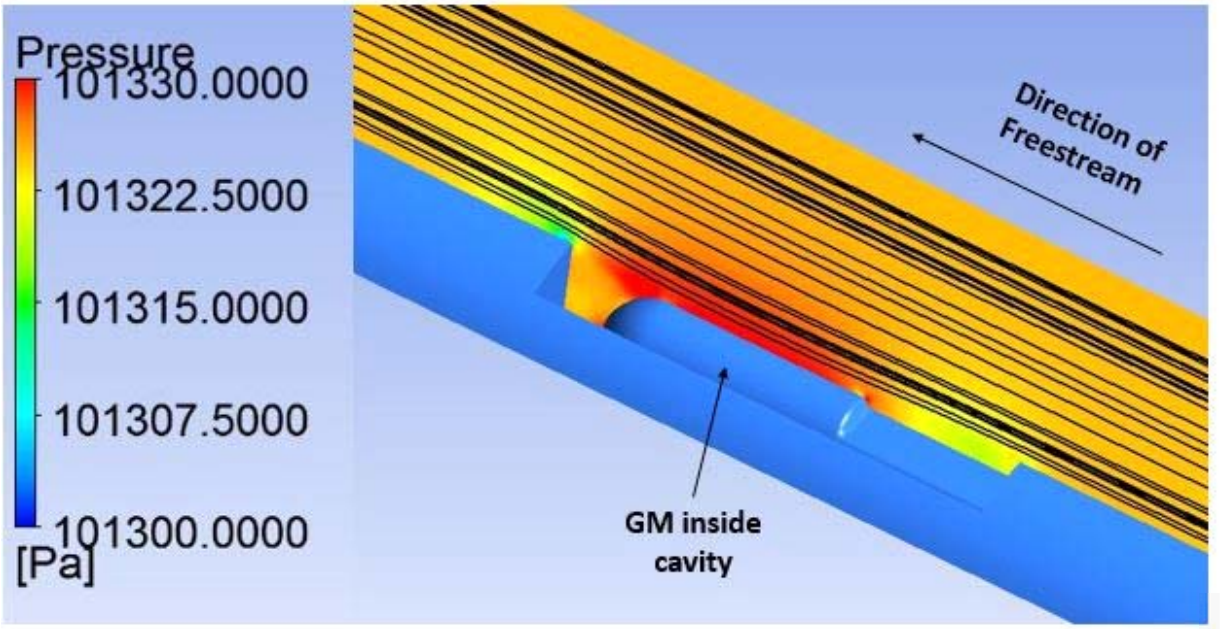

Figure 47. Configuration1 CFX results.

Further analysis was performed to investigate the interaction of the GM in the freestream at the moment when the kickers were fully extended. This moment was important for understanding how the GM would actually leave the rocket body. The back-end first deployment method was predicted to face large pressures pushing the GM back into the cavity since it represented a blunt body being pushed into freestream flow; the high pressure stagnation region on the GM surface slows down the flow, while the low pressure recirculation region within the cavity could possibly pull the GM back inside.

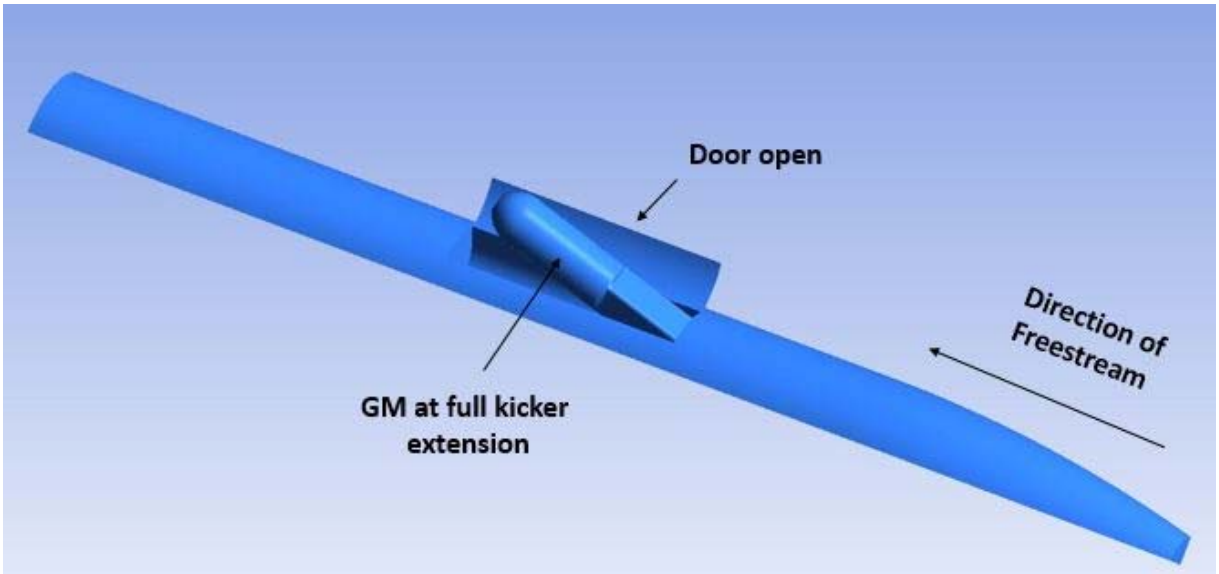

Figure 48. CFX Configuration 2: Doors open and GM at full kicker extension.

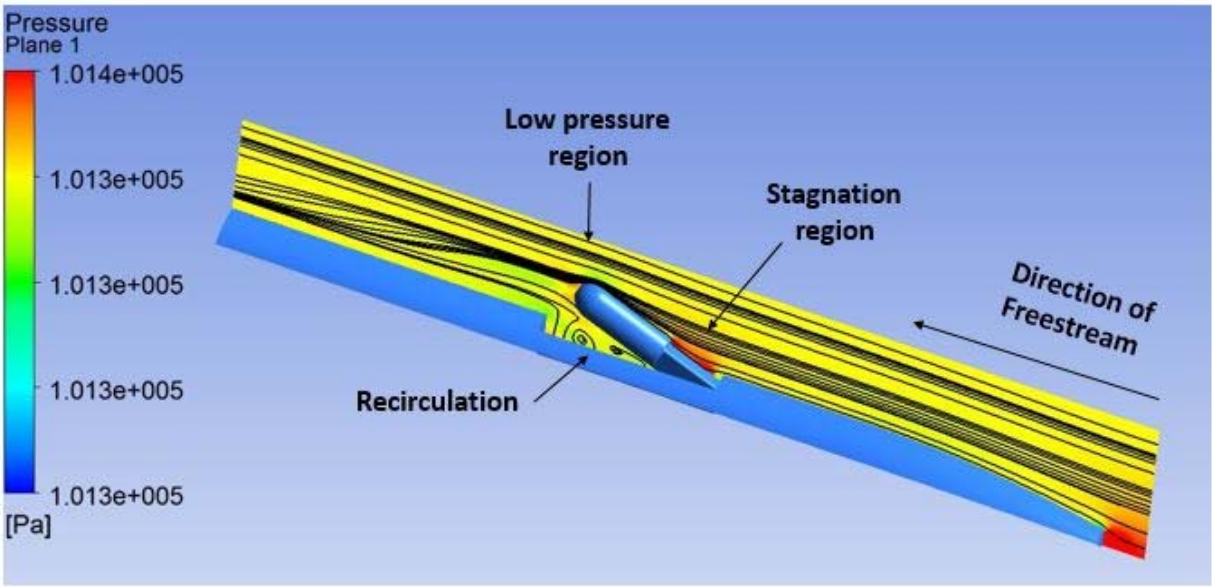

Figure 49. Configuration 2 CFX results.

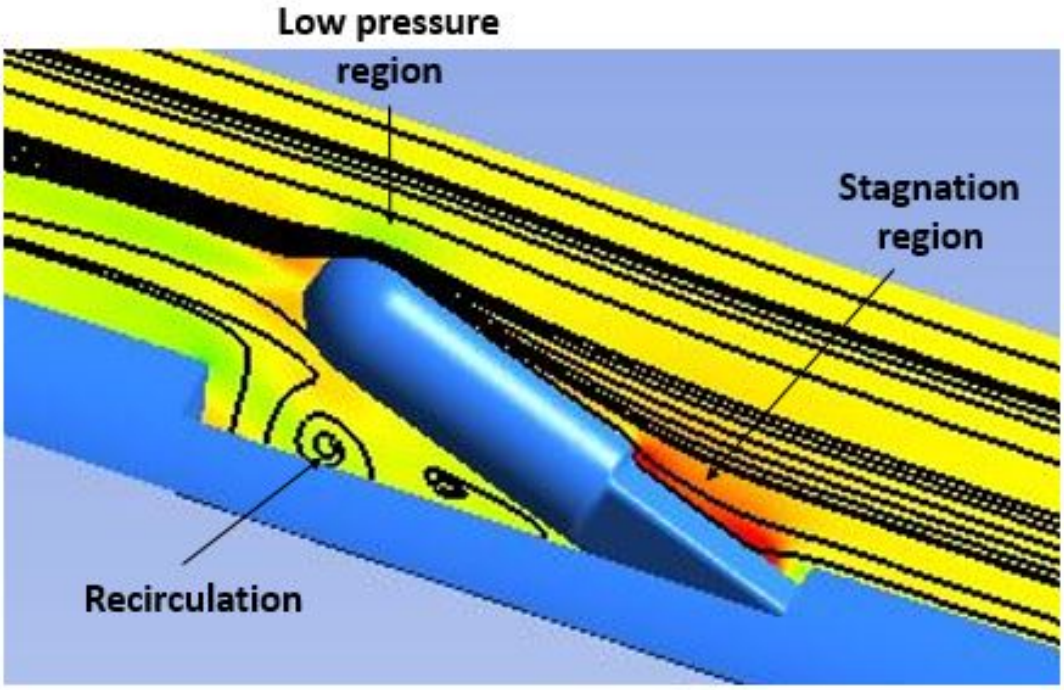

Figure 50. Figure 50, Immediate GM flow field.

The CFD analysis highlighted the recirculatory region as expected, with slightly lower pressure than ambient. However, a high-pressure region was shown to develop on the lower faces on the GM and a low-pressure region existed on the top of the GM nose cone. This region of lower pressure was unexpected but makes sense since the flow appears to significantly accelerate around the GM nose cone. The high and low pressure couple acting on the GM actually created a moment pushing the GM out of the cavity.

The kickers were designed to remain fully extended after actuation due to the inherent weight of the assembly and residual pressure force of the piston and restrict the GM from being sucked back in the cavity. Following the CFD analysis, the final design could likely be necessary due to the GM geometry and moment created. The fully extended kickers would remain as a redundancy to ensure that the GM should not reenter the cavity.

4. Final Modifications

The successful ground test meant that the deployment mechanism was ready to be tested during flight, and the CFD analysis verified the design during flight conditions. The entire SUAVE vehicle was outfitted with slight modifications for improved durability to prepare for a full-scale launch. The modifications included:

- Aluminum disk installed upon piston stopper
- Parachute bulkhead extended away from CO_2 bulkhead using all-thread rods for improving the parachute load path
- Aluminum struts installed longitudinally between the door cavities to prevent buckling

The aluminum disk addition to the piston stopper was described above in III.C.2 and is shown in Figure 45. A different bulkhead with a U-bolt was created to protect the electronics which deployed the piston from the parachute recovery system. This bulkhead was called the parachute bulkhead. Initially, the CO_2 bulkhead was outfitted a U-bolt itself and would be directly connected to the parachute, but the risk of tearing the canvas upon separation was deemed too high. The CO_2 bulkhead was instead modified with two all-thread rods that would allow the parachute bulkhead to sit 4 inches above the CO_2 bulkhead and restrict the parachutes access to the CD3 system and two Perfect Flight altimeters below. The all-thread rods would also transmit the high axial drag loads from the unfurled parachute to the CO_2 bulkhead, which was secured to the rocket both with eight 19.05 mm (0.75 in) machine screws for added support.

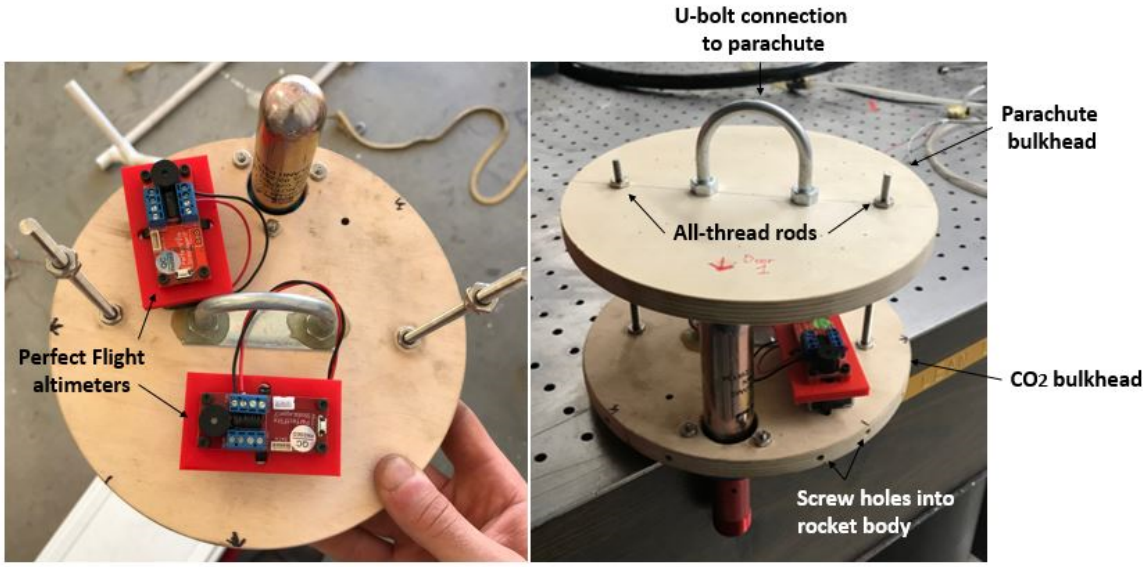

Figure 51. CO_2 bulkhead (Left) and parachute bulkhead attachment (Right).

External aluminum struts were installed in between the door cavities to transfer the axial vehicle load around the GM housing to eliminate a buckling failure. The removal of four door cutouts from the rocket body severely diminished the strength of the tubing during high acceleration loads and bending moments. Events that could cause severe axial loads upon the GM bay include the initial thrust impulse upon launch, when all components forward of the thrust wall experience compression, and during parachute deployment when all the components experience tension. A "snatch" load also occurs when the parachute builds up a sizable difference in velocity compared to the rocket [42], which when multiplied by the parachute mass results in significant momentum away from the rocket. The cord connecting the parachute to the rocket will cause a sudden whip-load down the cord which can be up to two times the load after the parachute opens [42]. Shock cord was used for this connection in attempts to dissipate a portion of the snatch load through elastic stretching.

Using shock cord would diminish the snatch load, but the four door cutouts 4 inches in arc length each decreased the cross sectional area of the fiberglass tubing in the door section from 0.61 m (24.19 in) outer radius to 0.21 m (8.19 in). The tubing that

would experience tension during parachute deployed loses 66.14% of circumferential support in the GM housing section, meaning each remaining sliver of tubing would absorb an additional 9% of the surrounding axial stress. The aluminum struts add an extra material component of strength in case the fiberglass tubing yielded under the increased load since the aluminum struts have a higher tensile strength than the thin layer of fiberglass wrapped around phenolic tubing and also increase the cross-sectional inertia for stiffness.

Inertial bending moments could also cause the door slivers to buckle during flight. The most severe bending moment would occur from a large gust of wind which mimics an angle of attack and induces lift on the tail fins and nose cone. The rocket's inertia would be the only restraint to these aerodynamic loadings in the lateral plane since the rocket can be assumed to be in dynamic equilibrium [43]. Objects with mass within the rocket would have the tendency to produce a load in the opposite direction of the vehicle acceleration.

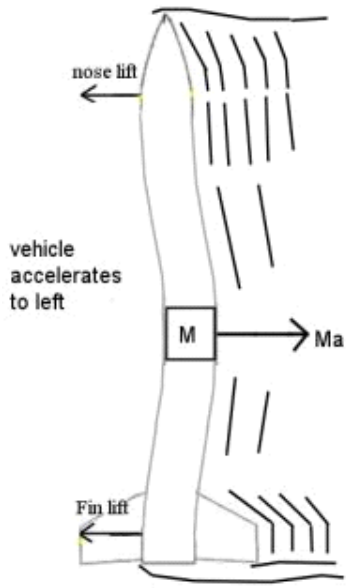

Figure 52. Inertial loads caused by wind gusts. Source: [43]

The most massive section within the upper stage would be where the GMs are housed, so the bending moments exaggerated in Figure 52 would laterally stress the door slivers severely. The aluminum struts were cut to extend past the door opening 2 inches on top and bottom, which would allow the stiffness of the strut to take the load from the rocket body and prevent structural failure during these high loading. Since the aluminum struts were required to be located on the outside of the rocket body as opposed to the inside due to the piston and kicker bulkhead locations, the struts would protrude 61.44 cm (0.5 in) from the body and interact with the freestream flow. Small triangular inserts were 3-D printed to minimize the flow disturbance from the struts and allow air to flow relatively smoothly across the GM bay. The aluminum strut locations and triangular inserts are shown below in Figure 53. The entire SUAVE vehicle was ready to be assembled save the nose cone which would be modified with a forward-looking camera housing for a GoPro Hero Session 5.

Figure 53. Aluminum strut fortifications added to GM bay.

THIS PAGE INTENTIONALLY LEFT BLANK

IV. TARGETING HUB ANALYSIS

A. MISSION ANALYSIS

1. Overview

The utility of the SUAVE vehicle for the counter-swarm mission lies not only in munition deployment at altitude but also the capability to localize and track the enemy swarm and guide the GMs to their targets. This far-reaching capability requires a centralized architecture consisting of a main targeting hub which detects and processes a target field and then relays guidance information to numerous GM nodes the target position and orientation (pose) from the targeting hub. The targeting hub would be placed in the SUAVE nose cone so that once the upper stage rotated downward following apogee, the targeting hub would initially have a wide perspective of the falling GMs and enemy swarm. The canopy size would dictate the targeting hub rate of descent, in which a slower, stable descent would yield a larger field of view (FOV) for a longer amount of time.

This centralized architecture was selected to minimize the complexity of systems required onboard the GMs. The targeting hub would resolve the pose of both the GMs and the enemy swarm, and the GMs would solely be sent fin commands to direct towards the moving target. By placing the sensing and control processes into the nose cone, the GMs are more expendable thus less expensive and easier to reproduce. This aligns with both the cost-symmetry and reproducibility missions of the SUAVE vehicle: the more valuable and complex targeting hub drifts down under canopy to be retrieved for future usage while the low-cost munitions are sent to combat the swarm and trigger a proximity-fused net to envelope the enemy UAV. A high-level overview for the tracking system within the targeting hub was created by identifying the major components necessary to achieve this capability. This surface sweep would require future work specialized in control systems to realistically implement these components into the SUAVE vehicle. Additionally, information would be gathered during a flight test to provide insight on the nose cone FOV and stability for use in future targeting hub analysis.

2. High-Level Control Design

The three guidance techniques that military missiles typically use are command guidance, homing guidance, or navigational guidance [44]; the guidance technique selected is determined by the intercept scenario for each specific missile. Homing and navigation guidance systems, which include proportional navigation and pursuit guidance missiles, are similar in that they rely on complex sensors and guidance computers within the missile itself to measure disparities between the missile heading and line of sight (LOS) from missile to target. Different control laws can be implemented to orient the missile towards the target or towards a calculated intercept point [45]. The missile in the SUAVE mission architecture is the GM, which was specifically designed to be inexpensive and relatively disposable compared to the more complex targeting hub. A complex seeker and guidance computer within the GM for homing/navigational guidance would defeat the low-cost mission, as each deployment of four GMs would result in the destruction of four sensor/guidance systems. As mentioned above, the sensors and electronics would be placed in the nose cone targeting hub which sends commands to the GMs; a command guidance architecture, specifically a variation to the semi-automatic command to line of sight (SACLOS) would most closely fit the mission profile.

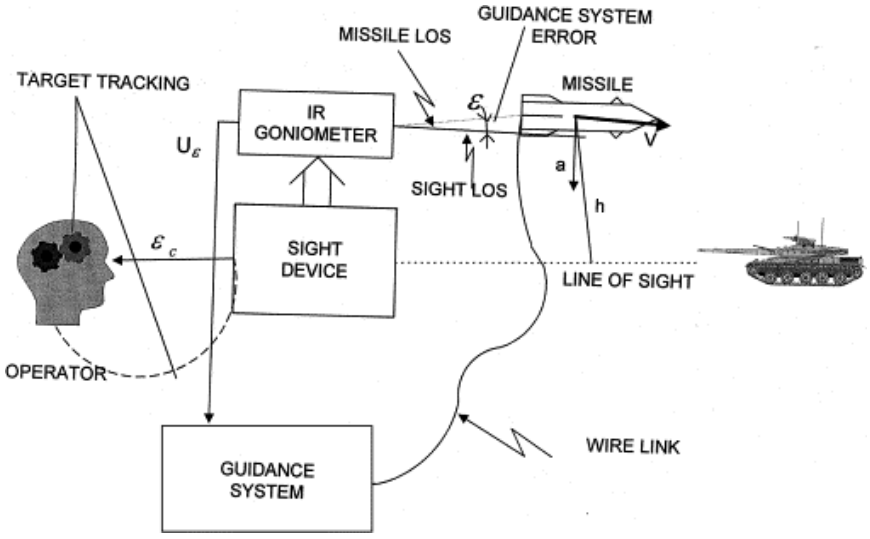

Figure 54. Semi-automatic CLOS guidance system. Source: [46]

SACLOS guided machines consist of a sighting component that fixes onto the target and directs the missile to stay in that LOS until the target is neutralized. Two cameras are used in each system: a wide field of view lens used to locate the missile immediately after launch and a narrow FOV lens with automatic zoom to provide the fine missile adjustments [46]. However, SACLOS requires an operator to keep the sighting component fixed upon the target. In the SUAVE scenario, the targeting hub would be pointed straight down and would have no user in the loop, so the camera would have to be gimbaled to keep the target UAV in the center of the crosshairs. As the GM fell, the narrow FOV lens would translate the emitted signals, each individually addressed in the FOV, into an electrical impulse, which would change as the GM location left the center of the crosshairs; electronics would then automatically send correction commands in the opposite direction [46]. The GM would be outfitted with a unique beacon transmitter to be extremely bright for visual location using a strobe or high-power LED or laser, so it would be centered back onto the LOS between targeting hub and target using commands that would be sent using radio frequencies. Radio guided missiles are more susceptible to jamming than other SACLOS guidance command links such as wires, however using wire-guidance was deemed to be impractical due to possible interference with doors and rocket body during ejection.

Gimbaling the camera to keep the target UAV in the crosshair would have to be solved in order for this design to be effective. The Perceptor Dual Sensor gimbal from Lockheed Martin was designed for high quality imaging and target tracking of small UAVs [47]; the gimballed tracking technology from the Perceptor would be a strong reference for what is needed on the targeting hub. The SACLOS dual-lensed cameras mentioned previously would be integrated into the gimbal housing to complete the targeting hub sensor system.

Figure 55. Lockheed Martin Perceptor Dual Sensor gimbal. Source: [47]

Each GM would require the targeting hub to have one imaging system with a dual lens for sighting the target and tracking the GM, one gimbal housing to allow the camera to rotate freely, and one antenna for downlink transmission of guidance commands. For a complete payload load out, the targeting hub would be equipped with four separate camera/antenna systems. The guidance system and goniometer would be located within the nose cone body along with the power supply. The GM would ideally be guided along the LOS of the targeting hub and the target until collision with the threat. However, since the CLOS is generally used for midcourse guidance due to the increased acceleration demands during terminal phase close to the target [48], the benefit of the SUAVE kill mechanism would be the large net that it expels when in proximity of an enemy UAV. The GM would be programmed to fire the net at a specified distance from the UAV to avoid significant acceleration demands at intercept.

B. 11 MAY 2019 LAUNCH

1. Preparation and Launch

To realistically succeed in creating a targeting hub with the capabilities outlined above, each aspect of the high-level design will have to receive more specialized and detailed design attention. Beyond the GM deployment design, this thesis attempted to test both the sensor FOV and nose cone stability metrics of this particular SUAVE vehicle during flight to pass on information useful for the further development of the targeting hub. A camera housing was designed to be placed at the end of the nose cone to mimic the gimballed camera sensor which would track the GMs during descent. A GoPro Hero 5 Session camera was used as the initial sensor in this configuration. The camera housing structure followed the tangent ogive curve calculated in Appendix A. To increase the distance that the GoPro would be capable of resolving the GMs, each munition was painted fluorescent orange and outfitted with reflector tape to better establish themselves against the desert floor. This mimicked the flares that would be attached to the GM in the actual configuration.

Figure 56. GMs with fluorescent paint and aft end reflectors.

Figure 57. Nose cone camera housing for GoPro Hero 5 Session.

The video feed of the nose cone camera would define the FOV limits of any sensor placed on the nose cone, as well as the targeting hub stability in this configuration. This information would be critical for future sensors installed onto the nose cone. The nose cone was installed onto the GM bay and was outfitted with parachutes. The vehicle used a Cesaroni L610 as the solid rocket motor for flight. The final rocket design and structure is shown below in Figure 58.

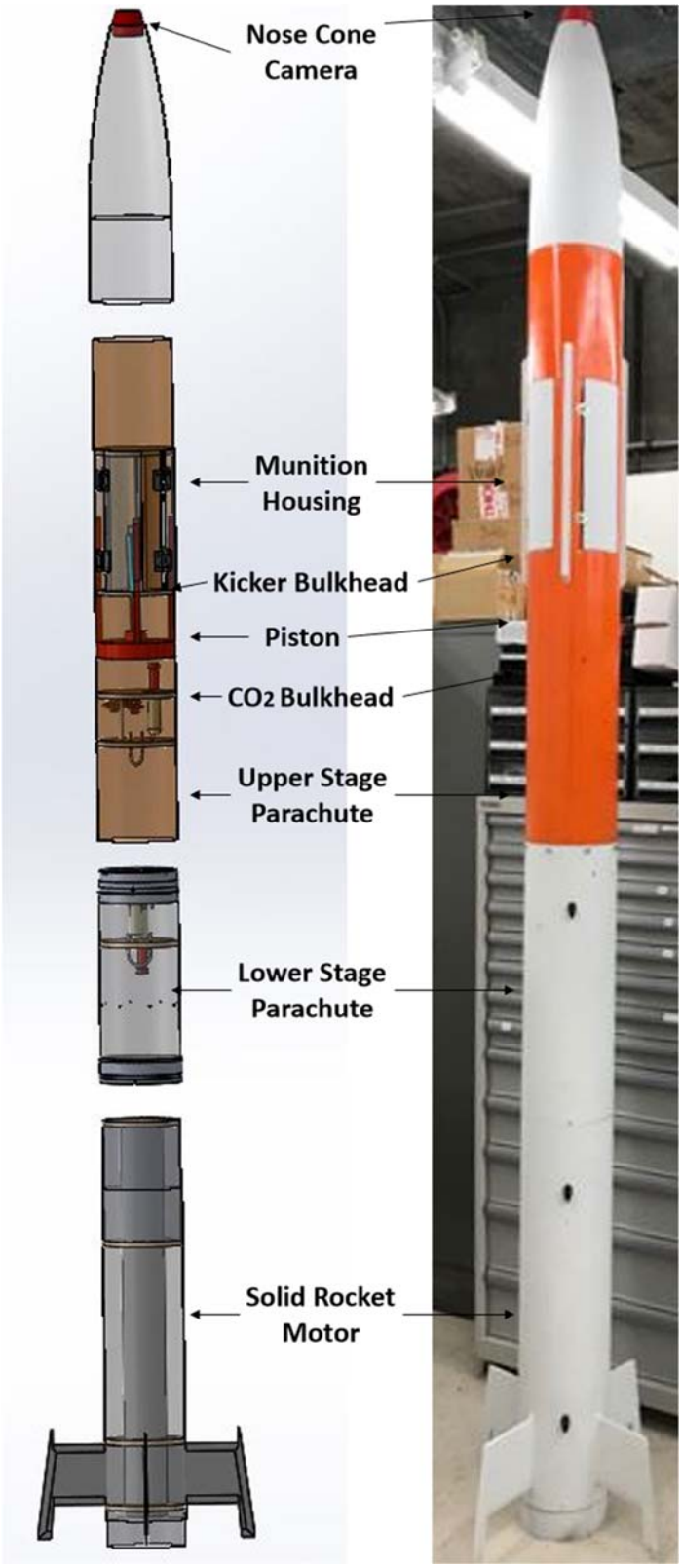

Figure 58. Final SUAVE vehicle.

The final flight occurred on the morning of Saturday, 11 May 2019, at the Friends of Amateur Rocketry site in the Mojave Desert. Launch goals included verifying the multiple GM deployment mechanism and gaining aerial footage from which required FOV and stability can be resolved. Additionally, the condition of the SUAVE vehicle on recovery was desired to be in working order with no major failures. The deployment mechanism would be verified if the doors opened at the specified time (apogee + five seconds) and did not open prematurely. A successful launch would also have the nose cone camera able to resolve the falling GMs. This was necessary for the project to move forward into the next stage since visual contact of the GMS would establish the likelihood of a visible/near infrared link between the GM deployment phase and the targeting hub guidance/control phase.

2. Flight Results

The vehicle reached an apogee of 1037.23 m (3403 ft) AGL in 18 seconds and separated into the upper stage and lower stage. The lower stage descended until the main "B" parachute was deployed at 274.32 m (900 ft) AGL while the upper stage pivoted and began accelerating downwards. Five seconds following apogee, the 25 gram CO_2 cartridge burst and drove the piston towards the kicker bulkhead. The doors did remain secured following apogee separation as seen from the lower stage.

Figure 59. Upper stage with closed doors as seen from lower stage.

The pressure relief vent-hole calculations were demonstrated to be adequate as the piston did not actuate prematurely and open the doors. Additionally, the strength of the neodymium magnets on the piston legs was enough to hold the doors closed during the launch phase of the flight. The GMs were successfully deployed five seconds after apogee at an altitude of 975.36 m (3200 ft) as scheduled, and the nose cone camera was able to visually resolve the GMs falling away for two seconds.

Figure 60. First view of GMs from nose cone camera.

The GMs were lost from sight after the two second period, as they descended at a quicker rate and became undiscernible against the desert floor. The descent rate of the nose cone was calculated from the Perfect Flight altimeter data to be 6.46 m/s (21.19 ft/s), while

the GM descent rate was estimated to be 68.81 m/s (225.75 ft/s). This high-end estimation was calculated using the follow assumptions and simplifications:

- GM reached terminal velocity immediately following deployment
- Drag coefficient (C_d) was assumed to resemble that of a blunt bullet: 0.295 [49]

The weight of the GM was measured to be 0.2925 kg, which resulted in a weight of 2.8665 N. At terminal velocity, the force due to gravity was equal to the drag force acting against the GM. This drag force of 2.87 N was used along with the assumed C_d and ambient density to determine the terminal velocity of the GM. After two seconds, the differing descent rates of the nose cone and the GM would result in an altitude difference of 124.7 m (409.12 ft). The oversimplification of constant terminal velocity of the GM made the calculated resolution distance a best case scenario. The absolute maximum resolution distance of the targeting hub camera was 124.7 m (409.12 ft), but was most likely slightly shorter. Future development of the targeting hub would not consist of using a GoPro camera as the main sensor, but this resolution distance highlights the necessity for greater signal-to-noise and reflectivity of the GMs moving forward. This could be achieved with high power pulsed light emitting diodes (LEDs) along with narrow band pass filters on the imaging camera.

The data from the GoPro was also analyzed for stability and field of view purposes. Unless the sensor system required the targeting hub to be rotating, such as in the Rolling Airframe Missile, the nose cone would be required to descend with zero rolling moment and minimal pitch and yaw movements to keep focus on the GMs below. Rotation of the nose cone would also tangle the parachute lines and potentially affect the rate and direction of descent, so roll stabilization would have to be incorporated. Weighting the nose and extending the length and connection design of the parachute tether were methods tested to determine the feasibility of roll stability without a complete closed loop control system.

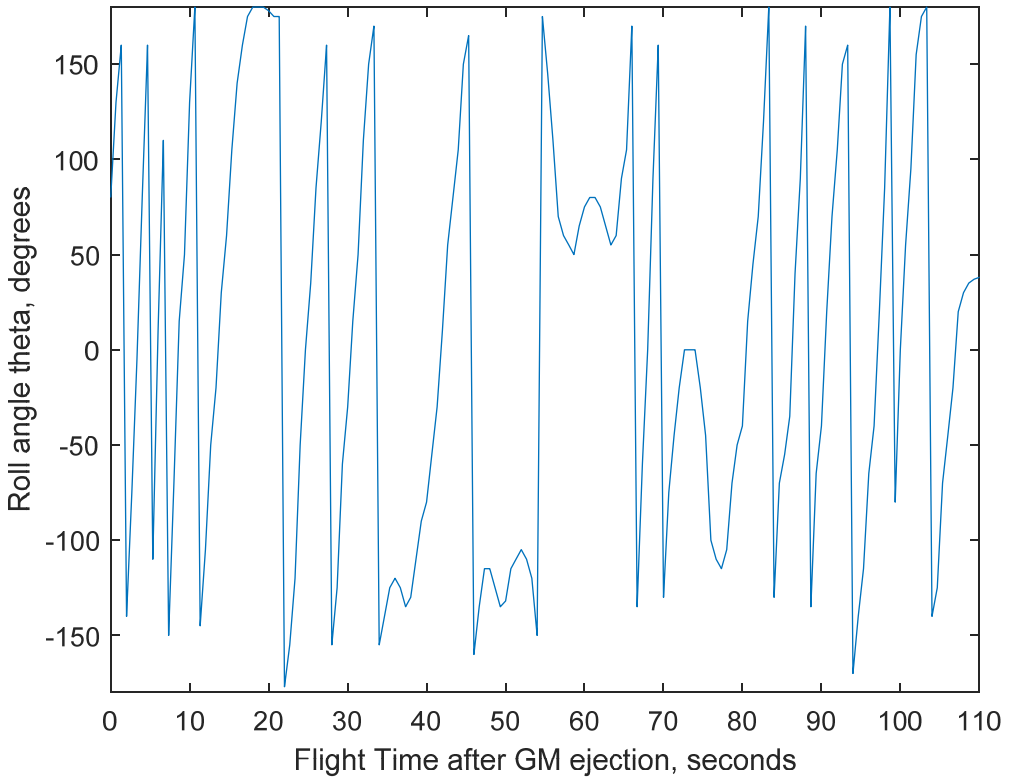

Figure 61. Plot of nose cone roll angle orientation during descent.

The nose cone proved to roll significantly upon descent, as shown in Figure 61. The vehicle completed 15 full rotations during the 110 second descent, reaching a maximum roll rate at one point of 0.5 revolutions per second. The average roll rate during descent was 0.2 revolutions per second.

The field of view from the GoPro vantage point in the nose cone was calculated using two different photographs at different altitudes. The FAR site outline was visible during descent, and the actual dimensions of the landmarks were found using satellite imagery. The known length landmark quantities shown in Figure 62 were measured and scaled to match the photograph frame measurements. The lateral field of view was found using the arctangent function of half lateral frame dimension divided by the altitude. Similarly, the vertical field of view used trigonometry with half of the vertical frame

dimension and altitude. The altitudes were known based on the time stamp of the photograph and the descent rate of the targeting hub. Two photographs were analyzed to provide an average FOV for both channels from the GoPro camera; the calculations are shown in Appendix B.

Figure 62. Friends of Amateur Rocketry site dimensions.

Table 5. Field of view measurements.

Timestamp after Apogee (s)	Altitude (m)	FAR East side measurement (cm)	FAR South side measurement (cm)	Lateral FOV	Vertical FOV
0	975.36	5.72	6.35	54.63°	46.46°
36.667	738.54	6.67	8.57	55.96°	48.07°
			Average	55.30°	47.26°

The GoPro camera had a total field of view of 55.30˚ by 47.26˚. A more important metric for future work however was the maximum angle FOV angle that would contain the GMs during the entire descent. This angle would dictate how wide the targeting hub sensor would need to see at a minimum to visually identify the GMs; this FOV would be smaller than the wide angle FOV from the GoPro, allowing future designers to decrease the sensor FOV capability to increase the resolution. The distance between the left GM in Figure 63 and the center of the photograph was measured and scaled to feet on the ground track. The left GM was used as opposed to the right GM to measure maximum angle necessary to resolve both. The first frame was assumed to be adequate for this analysis, as the FOV angle around the GMs would decrease as they fell farther from the targeting hub. Similar trigonometric calculations as previously mentioned were made using the known altitude to result in a minimum FOV angle of 40.92˚ to resolve both GMs.

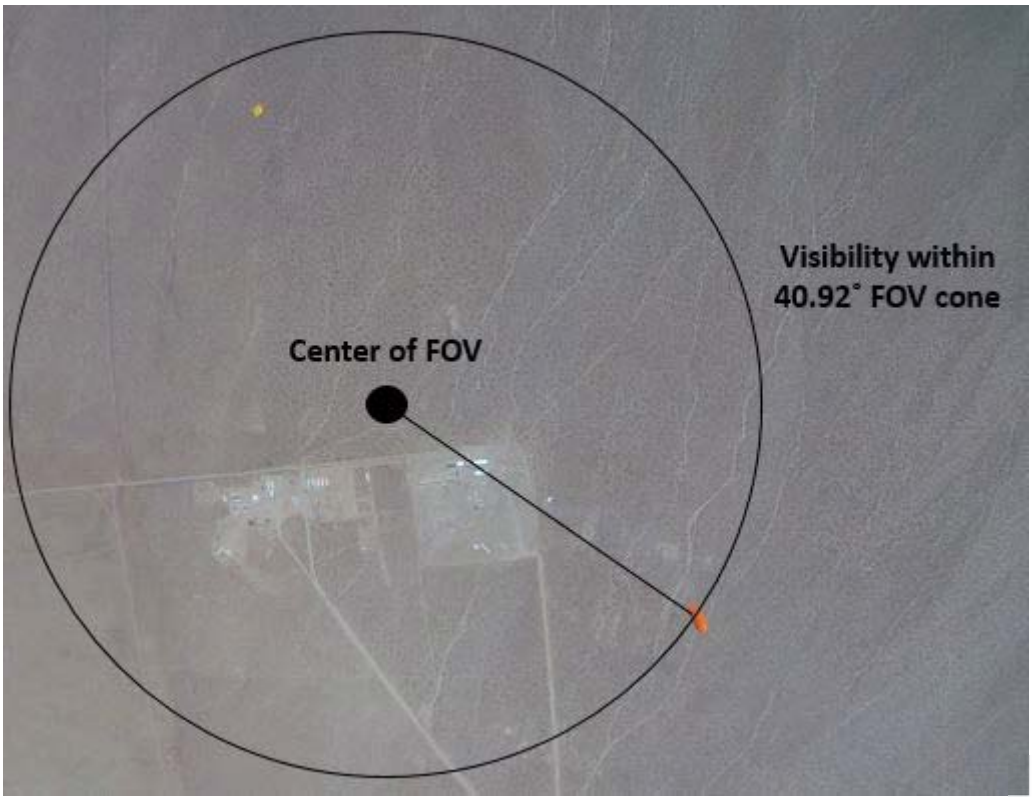

Figure 63. Minimum field of view angle required to resolve GMs.

The final launch proved to be a successful gathering of data for future work on the SUAVE vehicle. The rocket remained stable during ascent, and the deployment mechanism functioned flawlessly to eject the GMs at the specified time. The data gathered included:

- The targeting hub acquired the GMs for two seconds and for a maximum distance of 124.7 m (409.12 ft)
- The targeting hub rolled at an average of 0.2 rotations per second in the negative (counter clockwise) direction
- The minimum FOV angle needed to resolve both GMs was 40.92˚

Lessons learned for the launch that would be used moving forward would be the need for more visibility for the downward-looking camera; this would be achieved by improving the camera imaging quality as well as adding an actively pulsed emission source to the aft end of the GM for stark resolution.

V. COST

The most important facet of the SUAVE project is with regards to cost. Lethal UAVs that are produced at a fraction of the cost compared to the weapons that defend against them create a very asymmetric advantage for less-powerful state and non-state actors, particularly terrorist organizations, against the United States and her allies. The capability that the SUAVE vehicle provides is neutralization of a swarm threat using a system that is comparable in production price to the UAVs themselves.

The delivery vehicle lower stage booster and control mechanisms designed by Capt. Kai Grohe (RCAF) were estimated to cost $4300 [14], and the guided munition designed by Robert Wright and Capt. Keith Lobo cost an additional $625 to design and construct [15]. The GM bay and targeting hub nose cone was constructing using a majority of in-house rocket body materials and 3-D printed parts making an accurate cost estimate difficult. The parts purchased for this thesis and their respective costs are shown below in Table 6. This thesis added an addition $1233.69 to the project, not including 3-D printed components and labor, bringing the estimated total cost for four GM deployment up to this point to approximately $8033.69.

Table 6. GM bay and targeting hub approximate costs.

Component	**Qty.**	**Unit Cost ($)**	**Total Cost ($)**
Perfect Flight StratoLoggerCF Altimeter	2	61.06	122.12
GoPro Hero Session 5	3	154.99	464.97
Door spring	8	0.87	6.99
Neodymium magnet	8	1.25	9.99
12.7 mm thickness wood bulkhead	3	8.39	25.17
25 g CO_2 cartridge and CD3 ejection system	1	222.01	222.01
7.62 cm diameter phenolic tubing – 91.44 cm length	2	21.95	43.90
19.05 cm diameter pre-glassed phenolic airframe tubing – 121.92 cm length	1	199.99	199.99
Aluminum U-Channel – 2.44 m length	1	16.76	16.76
19.05 cm diameter Fiberglass Nose Cone	1	121.79	121.79
		Total Cost:	$1233.69

As the project is iterated to ultimately achieve success neutralizing UAV threats, more costs will be required, realistically eclipsing the $10,000 mark. A project that has a price tag on that order of magnitude remains extremely attractive compared to the hundreds of thousands to millions of dollars that defense missiles cost per unit. The mission architecture of the SUAVE vehicle values the expected reusability of the robust targeting hub, which is predicted to be the most expensive part of the vehicle, and minimizes the cost of the expendable munitions; the long mission life capability of each SUAVE vehicle significantly drives the price per target neutralized down to a level symmetric with the swarm costs themselves.

VI. CONCLUSION

A. SUMMARY

A mechanism for deploying multiple munitions from the SUAVE vehicle moving at flight velocities was designed, built, and tested. The research effort extended existing work done on the SUAVE project at the NPS Rocket Propulsion Lab, and contributed important designs and metrics that will be used for furthering the project. The main objectives outlined at the beginning of the project were satisfied:

Single munition deployment was the first task accomplished and the February 2019 launch verified that a munition deployed at apogee could be controlled using remote-guidance during descent.

The second objective regarding multi-munition deployment was achieved by extending capabilities from one munition to multi-munitions to drive down the operational costs to combat UAV swarms; more expendable munitions would increase the SUAVE capability to target enemy UAVs and decrease the overall price per target neutralized. Multi-munition deployment required analysis and testing to adequately construct a mechanism capable of ejecting a munition on the ground. Computational fluid dynamics validated the GM bay design in a flight scenario and led to the successful May 2019 launch in which the GMs were ejected at the specified time.

Visually identifying and tracking the GMs during descent was the third objective of the project, and was adequately achieved during the May 2019 launch in which the GMs were seen falling following deployment from the SUAVE vehicle. Useful metrics regarding nose cone stability and field of view parameters necessary for GM tracking were collected and would be beneficial for future targeting hub research.

B. FUTURE WORKS

Future iterations of the SUAVE vehicle will mainly be focused on completing the timeline between GM deployment and target intercept. The high-level guidance design introduced in this thesis provides a starting point for more detailed research and analysis

into constructing a functioning targeting hub with the capability to direct munitions to a target UAV. This complex analysis will require sophisticated software and imaging tools able to anticipate swarm movement and track both the target swarm and the GMs simultaneously. Future SUAVE guidance and control systems would be greatly assisted using partnerships with other NPS laboratories including the CRUSER drone swarm team as experimental testbeds for swarm detection and intercept.

The deployment mechanism itself, including the piston, kickers, GM housing, etc., could be built into a more robust system using more durable materials such as aluminum and carbon fiber as opposed to 3-D printed PLA plastics. The design could also be utilized for projects apart from the SUAVE mission, including being transformed into a high-altitude payload delivery vehicle to take the place of high-altitude balloons, or any number of projects that desire durable, reliable deployment of a payload to solve a problem.

APPENDIX A. TANGENT OGIVE CALCULATION

A tangent ogive shape is formed from a segment within a circle of radius ρ as shown in Figure 64, where ρ represents the ogive radius, r the cross-sectional radius of the nose cone base, and L the overall length of the nose cone from base to point.

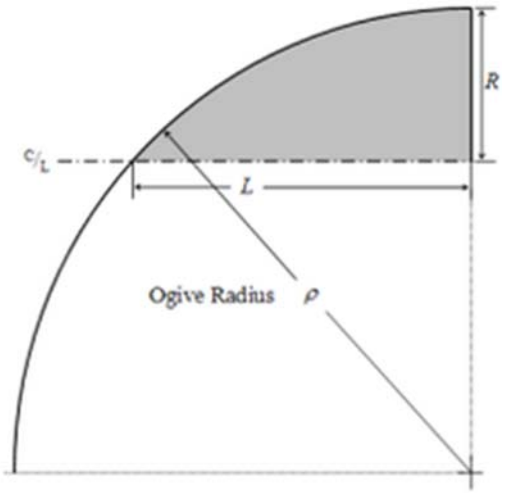

Figure 64. Tangent ogive cone geometry. Source: [50]

From geometry, the ogive radius ρ can be calculated as:

$$\rho = \frac{R^2+L^2}{2R} \qquad \text{Equation 9}$$

The exact length dimension of the nose cone used during flight was unknown, since several inches of the tip had been removed. The known length of the nose cone was measured at 18.5 inches, so this represented the variable L in Equation 9. The bottom outer diameter was measured to be 7.75 inches, and the top outer radius where the GM was located measured 3.125 inches. The R value used for calculation was the difference of the two diameters divided by 2: 2.313 inches. By effectively shifting the midline L of the ogive to a position which accounted for the GM opening, the same ogive curve was able to be modeled as shown in Figure 65.

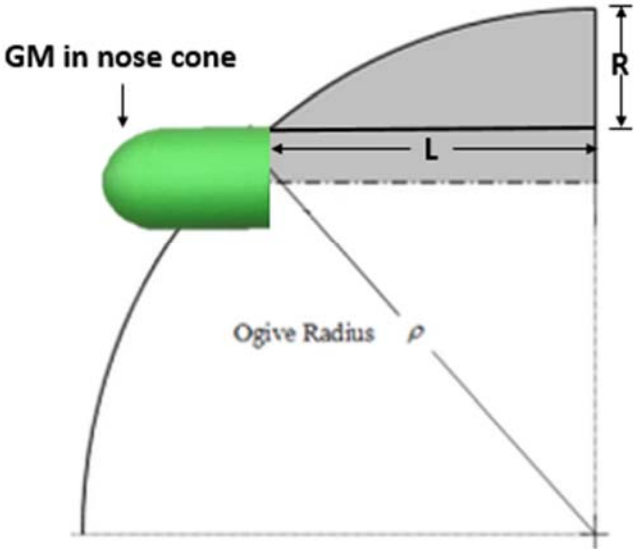

Figure 65. Actual tangent ogive curve determination with new radius and length.

In an X-Y coordinate reference frame, with L parallel to and placed on the positive x-axis and R in the direction of positive y, the value of any point on the ogive curve, y, for any x from 0 to L was:

$$y = \sqrt{\rho^2 - (L - x)^2} + R - \rho \qquad \text{Equation 10}$$

Equation 10 with measured values for R and L resulted in the following equation which was input into a SolidWorks model:

$$y = \sqrt{5306.2 + 37x - x^2} - 71.2813 \qquad \text{Equation 11}$$

APPENDIX B. MATLAB SCRIPTS

1. Tangent Ogive Calculations

```
%% For CFD analysis

r_opening = 1.5625;         % Radius at nose cone cut, in
l = 18.5;                   % Known length of nose cone, in
d = 7.75 - 2*r_opening;     % Diameter of nose cone end, in
r = d/2;                    % Radius of nose cone end, in

p = (r^2+l^2)/(2*r);        % Ogive radius, in

y1 = p^2 - l^2;             % First term in ogive equation
y2 = 2*l;                   % Second term in ogive equation
y3 = r - p + r_opening;     % Third term in ogive equation

syms x
y = sqrt(y1+y2*x-x^2)-y3;
pretty(y)                % Equation entered into SolidWorks

%% For Camera Housing

r_opening = 0;         % Radius at nose cone cut, in
l = 21;                   % Known length of nose cone, in
d = 7.75 - 2*r_opening;     % Diameter of nose cone end, in
r = d/2;                    % Radius of nose cone end, in

p = (r^2+l^2)/(2*r);        % Ogive radius, in

y1 = p^2 - l^2;             % First term in ogive equation
y2 = 2*l;                   % Second term in ogive equation
y3 = r - p + r_opening;     % Third term in ogive equation

syms x
y = sqrt(y1+y2*x-x^2)-y3;
pretty(y)                % Equation entered into SolidWorks
```

2. Electromagnet Calculations

```
% Rod type: Carbon steel from Home Depot
% Length of rod
k = 5000; % relative permeability (u/u0)
l_rod = 3.5; % inches
d_rod = 1; % inches

% Wire type: Magnet Wire from Amazon
% 30 AWG Copper
rho = (1.68e-6)/2.54; % resistivity in ohm-inches
d_copper = 0.0031; % inches
```

```
turns = l_rod/d_copper;
l_copper = (pi*(d_rod + 2*d_copper))*turns; % length in inches
% Remember that length with be longer due to leads
a_copper = 0.25*pi*d_copper^2; % CSA inches^2
r = rho*l_copper/a_copper; % Resistance in ohms

% Battery type: Li-Po
% Battery selection
voltage = (4.2)*1; % volts
current = voltage/r % current flowing through EM, amps

% Decide if this is enough to repel neodymium
u0 = ((4*pi)*10^(-7))*39.3701; % Tesla inches/amps
B = u0*k*(turns/l_rod)*current % Magnetic flux density, Tesla

%% Vectorized

data = xlsread('electromagnetic wire.xlsx'); % Reading in diameter and
max
                                               % current limits for
wire
                                               % gauge sizes 1 to 40
d_copper = data(:,2);                        % Wire diameters, in
max_current = data(:,3);                     % Wire max current limits,
A

% Rod characteristics
% Rod type: Carbon steel from Home Depot
u0 = ((4*pi)*10^(-7))*39.3701;               % Magnetic permeability of
                                               % free space, T*in/A
k = 100;                                     % relative permeability of
                                               % rod material (u/u0)
l_rod = ones(length(d_copper),1)*3.5;        % Rod length, in
d_rod = ones(length(d_copper),1)*0.5;        % Rod diameter, in


% Wire characteristics
% Wire type: Magnet Wire from Amazon
% 30 AWG Copper
rho = (1.68e-6)/2.54;                        % Copper resistivity, Ohm-
in
turns = l_rod./d_copper;                     % Number of turns on EM
l_copper = (pi*(d_rod + 2*d_copper)).*turns; % Wire length, in
a_copper = 0.25*pi*d_copper.^2;              % Wire CSA, in^2
r = rho*l_copper./a_copper;                  % Resistance through
wire,ohms


% Battery Characteristics
% Battery type: Li-Po
voltage = (4.2)*ones(length(d_copper),1);    % Battery voltage, V
current = voltage./r;                         % Current through EM, A
```

```
% Ampere's Force Law
B = u0*k*(turns./l_rod).*current             % Magnetic flux density, T
% Compare B to 0.378 T needed to negate Neodymium magnet

% Comparison of current allowed vs. current actual in wire gauges 1 to
40
figure(1)
plot(d_copper,current,d_copper,max_current)
legend('Actual Current','Allowable Current')
xlabel('Copper Wire Diameter, in')
ylabel('Current, A')
ylim([0,0.1])

% Magnetic flux density for wire gauges 1 to 40
figure(2)
plot(d_copper,B)
xlabel('Copper Wire Diameter, in')
ylabel('Magnetic Flux Density, T')
ylim([0,50])
```

3. Atmospheric Pressure Calculations

```
% Pressure forces due to changing altitude

% Paramters
h1 = 1655/3.281;     % Ground altitude, meters
h2 = 5465/3.281;     % Apogee altitude, meters
p0 = 101.325;        % Atmospheric pressure at sea level, kPa
T = 288.15;          % Standard temperature at sea level, K
g = 9.80665;         % Gravitational Acceleration, m/s^2
M = 0.02896968;      % Molar mass of dry air, kg/mol
R = 8.31582991;      % Universal gas constant, J/mol*k
SA = 44.1786;        % Surface area of piston, in^2

% Calculation for atmospheric pressure at ground altitude
p1 = p0*exp(-((M*g)/(R*T))*h1);   % Barometric Formula
p1 = p1/6.895;                    % Conversion to psi

% Calculation for atmospheric pressure at apogee altitude
p2 = p0*exp(-((M*g)/(R*T))*h2);   % Barometric Formula
p2 = p2/6.895;                    % Conversion to psi


deltaP = p1-p2;      % Pressure difference between ground and apogee
F = deltaP*SA        % Force acting on piston due to pressure delta,
lbf
```

4. Pressure profile vs. vent-hole area study calculations

```
% Define test configuration vent-hole diameters and areas
d1 = 0.125;             % Run 1: 2x 1/8" vent-holes
a1 = pi*d1^2/2;
d2 = 0.1875;            % Run 2: 2x 3/16" vent-holes
a2 = pi*d2^2/2;
d3 = 0.25;              % Run 3: 2x 1/4" vent-holes
a3 = pi*d3^2/2;
d4 = 0.25;              % Run 4: 4x 1/4" vent-holes
a4 = pi*d4^2;

% Read in test data from CTAP pressure transducer
run1 = xlsread('Run1.xlsx');
run1 = (run1 - 3.078)*7.80843;  % Convert from voltage to pressure, psi
run1 = run1*6.89476;            % Convert from psi to kPa
run2 = xlsread('Run2.xlsx');
run2 = (run2 - 3.078)*7.80843;  % Convert from voltage to pressure, psi
run2 = run2*6.89476;            % Convert from psi to kPa
run3 = xlsread('Run3.xlsx');
run3 = (run3 - 3.078)*7.80843;  % Convert from voltage to pressure, psi
run3 = run3*6.89476;            % Convert from psi to kPa
run4 = xlsread('Run4.xlsx');
run4 = (run4 - 3.078)*7.80843;  % Convert from voltage to pressure, psi
run4 = run4*6.89476;            % Convert from psi to kPa

% Parse data to only show pressure profile
x = 1:500;
run1 = run1(1:500);
run2 = run2(546:1045);
run3 = run3(3666:4165);
run4 = run4(2406:2905);

% Plot pressure profile vs. time for all test configurations
figure(1)
plot(x,run1,x,run2,x,run3,x,run4)
xlim([0,500])
ylim([0,40])
ylabel('Pressure, kPa')
xlabel('Time, ms')
legend('Run 1: 2x 0.32 cm','Run 2: 2x 0.48 cm','Run 3: 2x 0.64 cm','Run
4: 4x 0.64 cm')

% Create array of maximum pressure values for each test configuration
Max1 = [max(run1),max(run2),max(run3),max(run4)];
a = [a1,a2,a3,a4]*6.4516;

% Plot vent-hole areas and corresponding maximum pressure values
% achieved
figure(2)
plot(a,Max1,'*-')
ylabel('Pressure, kPa')
xlabel('Total vent area, cm^2')
```

5. Nose Cone Stability and Field of View calculations

```
% Nose Cone Field of View Analysis

% Point 1: altitude 3200'
east = 2.25;                    % FAR east side measurement, inches
south = 2.5;                    % FAR south side measurement, inches
altitude = 3200;                % Nose cone altitude, feet

% From Google Earth
east_act = 2727.14;             % FAR east side dimension, feet
south_act = 3136.53;            % FAR south side dimention, feet

east_ratio = east/east_act;   % Ratio between measured and actual, east
south_ratio = south/south_act;% Ratio between measured and actual,
                                 south
ratio = mean([east_ratio, south_ratio]); % Averaged ratio

frame_top = 7.3125;           % Photograph lateral measurement, inches
frame_side = 5.5;             % Photograph vertical measurement, inches
frame_lat_act = frame_top/ratio; % Actual lateral frame dimension, feet
frame_vert_act = frame_side/ratio; % Actual vertical frame dimension,
                                     feet

FOV_lat = atand((frame_lat_act/2)/altitude)% Lat field of view, degrees
FOV_vert = atand((frame_vert_act/2)/altitude)% Vert field of view,
                                               Degrees

% Point 2: altitude 1744.94'
east = 2.625;                    % FAR east side measurement, inches
south = 3.375;                   % FAR south side measurement, inches
altitude = 2423.026;             % Nose cone altitude, feet

% From Google Earth
east_act = 2727.14;             % FAR east side dimension, feet
south_act = 3136.53;            % FAR south side dimention, feet

east_ratio = east/east_act;   % Ratio between measured and actual, east
south_ratio = south/south_act; % Ratio between measured and actual,
                                  south
ratio = mean([east_ratio, south_ratio]); % Averaged ratio

frame_top = 7.3125;           % Photograph lateral measurement, inches
frame_side = 5.5;             % Photograph vertical measurement, inches
frame_lat_act = frame_top/ratio; % Actual lateral frame dimension, feet
frame_vert_act = frame_side/ratio; % Actual vertical frame dimension,
                                     feet

FOV_lat = atand((frame_lat_act/2)/altitude) % Lat field of view,
                                              degrees
FOV_vert = atand((frame_vert_act/2)/altitude) % Vert field of view,
                                                Degrees
```

THIS PAGE INTENTIONALLY LEFT BLANK

LIST OF REFERENCES

[1] "How Alan Turing cracked the enigma code," *Imperial War Museum,* Jan 5, 2018. [Online]. Available: https://www.iwm.org.uk/history/how-alan-turing-cracked-the-enigma-code

[2] V. C. Jones, *Manhattan, the Army and the atomic bomb*. Washington, D.C.: Center of Military History, U.S. Army, 1985. [Online]. Available: https://history.army.mil/html/books/011/11-10/CMH_Pub_11-10.pdf

[3] D. J. Bacon, *Second World War Deception: Lessons Learned for Today's Joint Planner*. Maxwell Air Force Base, Ala.: Air Command and Staff College, Air University, 1998. Available: http://www.au.af.mil/au/awc/awcgate/wright/wf05.pdf

[4] Z. Kallenborn, "The era of the drone swarm is coming, and we need to be ready for it," *Modern War Institute at West Point,* Oct. 25, 2018. [Online]. Available: https://mwi.usma.edu/era-drone-swarm-coming-need-ready/

[5] S. Wierzbanowki, "Gremlins," DARPA. [Online]. Available: https://www.darpa.mil/program/gremlins

[6] O. Pawlyk, "Pentagon still questioning how smart to make its drone swarms," Military.com, February 7, 2019. [Online]. Available: https://www.military.com/defensetech/2019/02/07/pentagon-still-questioning-how-smart-make-its-drone-swarms.html

[7] B. Xiang, "China launches record-breaking drone swarm," XinhuaNet, June 11, 2017. [Online]. Available: http://www.xinhuanet.com//english/2017-06/11/c_136356850.htm

[8] L. Yang, "Drone swarming technique may change combat strategies: expert," Global Times, February 13, 2017. [Online]. Available: http://www.globaltimes.cn/content/1032741.shtml

[9] E.B. Kania, "Battlefield singularity: artificial intelligence, military revolution, and China's future military power," Center for a New American Security, Washington, D.C., USA, November 2017. [Online]. Available: https://s3.amazonaws.com/files.cnas.org/documents/Battlefield-Singularity-November-2017.pdf?mtime=20171129235804

[10] A. Liptak, “A U.S. ally shot down a $200 drone with a $3 million Patriot missile,” The Verge, March 16, 2017. [Online]. Available: https://www.theverge.com/2017/3/16/14944256/patriot-missile-shot-down-consumer-drone-us-military

[11] T. Wright, “When is a drone swarm not a swarm?,” Air and Space Smithsonian, January 12, 2018. [Online]. Available: https://www.airspacemag.com/daily-planet/when-drone-swarm-not-swarm-180967820/

[12] “Head of the Russian General staff’s office for UAV development Major General Alexander Novikov holds briefing for domestic and foreign reporters,” *Ministry of Defence of the Russian Federation,* Nov. 1, 2018. [Online]. Available: http://eng.mil.ru/en/news_page/country/more.htm?id=12157872@egNews

[13] S. Roblin, “Can Russia’s Pansir air-defense system handle drone swarms?,” War Is Boring, December 12, 2018. [Online]. Available: https://warisboring.com/can-russias-pantsir-air-defense-system-handle-drone-swarms/

[14] K. Grohe, “Design and development of a counter-swarm prototype air vehicle,” M.S. thesis, Dept. of Mech. and Aero. Eng., NPS, Monterey, CA, USA, 2017. [Online]. Available: https://calhoun.nps.edu/handle/10945/56932.

[15] K. B. Lobo, “Submunition design for a low-cost small UAS counter-swarm missile,” M.S. thesis, Dept. of Mech. and Aero. Eng., NPS, Monterey, CA, USA, 2017. [Online]. Available: https://calhoun.nps.edu/handle/10945/61217

[16] K. Jones, interview, May 2018.

[17] F. D. Rydalch, “Missile demonstrator for counter UAV applications,” M.S. thesis, Dept. of Mech. and Aero. Eng., NPS, Monterey, CA, USA, 2016. [Online]. Available: https://calhoun.nps.edu/handle/10945/55204

[18] Math24, “Barometric formula.” Accessed May 23, 2019. [Online]. Available: https://www.math24.net/barometric-formula/

[19] “Bomb bay,” Wikipedia. Accessed May 23, 2019. [Online]. Available: https://en.wikipedia.org/wiki/Bomb_bay

[20] N.R.P., “F-35: the greatest American gamble,” Defencyclopedia, May 31, 2014. [Online]. Available: https://defencyclopedia.com/2014/05/31/f-35-the-greatest-american-gamble/

[21] BAE Systems, “Blackburn buccaneer,” 2019. [Online]. Available: https://www.baesystems.com/en/heritage/blackburn-buccaneer

[22] S. Atalay, “The transient cavity flow,” M.S. thesis, Dept. of Aero. Eng., Glasgow Univ., Glasgow, Scotland, UK, 2017. [Online]. Available: https://www.academia.edu/7629542/The_Transient_Cavity_Flow

[23] C. W. Dahike, “The aerodynamic characteristics of wrap-around fins at Mach numbers of 0.3 to 3.0,” U.S. Army Missile Command, Redstone Arsenal, Alabama, USA, 1976. [Online]. Available: https://apps.dtic.mil/dtic/tr/fulltext/u2/a036715.pdf

[24] G. K. Mandell, G. J. Caporaso, and W. P. Bengen, *Topics in advanced model rocketry*. Cambridge, MA: MIT Press, 1973.

[25] T. V. Milligan, “Why do spinning rockets fly straighter?,” Peak of Flight Newsletter, Issue 228, February 10, 2009. [Online]. Available: https://www.apogeerockets.com/education/downloads/Newsletter228.pdf

[26] E. C. Elko, J. W. Howard, R. C. Kochanski, T. T. Nguyen, and W. M. Sanders, “Rolling airframe missile: development, test, evaluation, and integration,” *Johns Hopkins APL Technical Digest,* vol. 22, no. 4, 2001. [Online]. Available: https://www.jhuapl.edu/techdigest/TD/td2204/Elko.pdf

[27] E. Tretkoff, “This month in physics history: Oersted and electromagnetism,” *American Physical Society*, vol. 17, no. 7, July 2008. [Online]. Available: https://www.aps.org/publications/apsnews/200807/physicshistory.cfm

[28] “Physics stack exchange,” April 4, 2017. [Online]. Available: https://physics.stackexchange.com/questions/323326/why-do-magnetic-field-lines-point-towards-the-north-pole-on-the-inside-of-a-sole?noredirect=1&lq=1

[29] “Magnetic domains & hysteresis,” Magic of Magnets, Northeastern University, Boston, MA, USA. Accessed April 30, 2019. [Online]. Available: https://www.ece.neu.edu/fac-ece/nian/mom/domains.html

[30] B. Lewczuk, G. Redlarski, A. Żak, N. Ziółkowska, B. Przybylska-Gornowicz, and M. Krawczuk, “Influence of electric, magnetic, and electromagnetic fields on the circadian system: current stage of knowledge,” *BioMed Research International*, vol. 2014, pp. 1–13, 2014.

[31] “Solenoid field from Ampere’s law,” HyperPhysics, Georgia State University. Accessed: May 23, 2019. [Online]. Available: http://hyperphysics.phy-astr.gsu.edu/hbase/magnetic/solenoid.html

[32] R. Clarke, “Magnetic properties of materials,” Surrey univ. workshop, August 2, 2008. [Online]. Available: http://info.ee.surrey.ac.uk/Workshop/advice/coils/mu

[33] "Magnetic field calculator," K&J Magnetics. Accessed: May 23, 2019. [Online]. Available: https://www.kjmagnetics.com/fieldcalculator.asp

[34] "Resistivity and temperature coefficient at 20 C," HyperPhysics, Georgia State University. Accessed: May 23, 2019. [Online]. Available: http://hyperphysics.phy-astr.gsu.edu/hbase/Tables/rstiv.html

[35] Learning RC, "RC LiPo battery guide: explanation, safety, and care," February 7, 2017. [Online]. Available: http://learningrc.com/lipo-battery/

[36] PowerStream Technology, "Wire gauge and current limits including skin depth and strength," April 19, 2019. [Online]. Available: https://www.powerstream.com/Wire_Size.htm

[37] T. V. Milligan, "Pressure relief holes," Peak of Flight Newsletter, Issue 68. [Online]. Available: https://www.apogeerockets.com/education /downloads/Newsletter68.pdf

[38] V. Knowles, "Altimeter port sizing," Vern's Rocketry. Accessed: May 23, 2019. [Online]. Available: http://www.vernk.com/AltimeterPortSizing.htm

[39] W. F. Phillips, *Mechanics of flight*. Hoboken, NJ: Wiley, 2010.

[40] *Rouse-Tech CD3 Instruction Manual,* Rouse-Tech, 2003. [Online]. Available: https://www.apogeerockets.com/downloads/PDFs/CD3_Manual2009.pdf

[41] G. Guo and Q. Luo, "DSMC investigation on flow characteristics of rarefied hypersonic flow over a cavity with different geometric shapes," *International Journal of Mechanical Sciences,* vol. 148, pp. 496–509, November 2019. [Online]. Available: https://www.sciencedirect.com/science /article/pii/S0020740318314437

[42] R. Newlands, "Parachute recovery system design for large rockets," Aspire Space technical papers, September 12, 2014. [Online]. Available: http://www.aspirespace.org.uk/downloads/Parachute%20recovery%20system%20 design%20for%20large%20rockets.pdf

[43] R. Newlands, M. Heywood, A. Lee, "Rocket vehicle loads and airframe design," Aspire Space technical papers, January 6, 2016. [Online]. Available: http://www.aspirespace.org.uk/downloads/Rocket%20vehicle%20loads%20and% 20airframe%20design.pdf

[44] "Guidance systems," Basic Science and Technology Section, United Kingdom Royal School of Artillery, February 15, 2003. [Online]. Available: https://web.archive.org/web/20070109230625/http://www.army.mod.uk/linkedfiles/royalartillery/units/royal_school_of_artillery/bst_handout_f02.pdf

[45] V. Dobrokhodov, "Introduction to missile guidance," class notes for ME4703 Missile Flight and Control, Dept. of Mech. And Aero. Eng., Naval Postgraduate School, Monterey, CA, USA, winter 2019.

[46] "Semi-automatic command to line of sight," Revolvy. Accessed: May 23, 2019. [Online]. Available: https://www.revolvy.com/page/Semi%252Dautomatic-command-to-line-of-sight

[47] "Perceptor dual sensor gimbal," Lockheed Martin Mission Systems and Training brochure, 2015. [Online]. Available: https://www.lockheedmartin.com/en-us/products/procerus-technologies/ perceptor-dual-sensor-gimbal.html

[48] K. Cosic et al., "Design and implementation of a hardware-in-the-loop simulator for a semi-automatic guided missile system." *Simul. Pr. Theory*, vol. 7, pp. 107–123, 1999. [Online]. Available: https://www.semanticscholar.org/paper/Design-and-implementation-of-a-hardware-in-the-loop-Cosic Kopriva/c3e642054f8b55c1943724a1b9bdd658f9d26 221

[49] N. Hall, "Shape effects on drag," NASA Glenn Research Center, May 5, 2015. [Online]. Available: https://www.grc.nasa.gov/www/k-12/airplane/shaped.html

[50] G. A. Crowell, "The descriptive geometry of nose cones," 1996. Accessed: May 23, 2019. [Online]. Available: https://web.archive.org/web/20110411143013/http://www.if.sc.usp.br/~projetosulfos/artigos/NoseCone_EQN2.PDF

THIS PAGE INTENTIONALLY LEFT BLANK

INITIAL DISTRIBUTION LIST

1. Defense Technical Information Center
   Ft. Belvoir, Virginia

2. Dudley Knox Library
   Naval Postgraduate School
   Monterey, California